Competitive Hardening Dynamics in Viscoplastic Materials with Evolving Threshold Stress

Yo-Lun Yang[a]

[a]*Graduate Institute of Manufacturing Technology, National Taipei University of Technology, Taipei, Taiwan*

Abstract

Conventional viscoplasticity frameworks treat the threshold stress as either a material constant or a quantity evolving solely with accumulated plastic strain. Since microstructural evolution — whether precipitation, phase transformation, or solute redistribution — may proceed concurrently with deformation, such a treatment is often inadequate. The present work formulates a constitutive framework, derived from the Clausius–Duhem inequality and Perzyna-type overstress viscoplasticity, in which the threshold stress evolves autonomously with physical time through microstructural kinetics, independently of accumulated strain. Modified Armstrong–Frederick kinematic hardening with static recovery is incorporated, so that back stress develops only during active inelastic flow. The interaction between time-driven threshold evolution and strain-driven back-stress development gives rise to three behavioural regimes: (I) a purely elastic response, (II) flow arrest, in which inelastic flow initiates but subsequently ceases as the threshold overtakes the effective stress, and (III) continuous flow. A constructive Lyapunov function is employed to prove that flow arrest is asymptotically stable, a result not previously established at the material-point level in the viscoplastic creep literature. It is further shown that back-stress development reduces the time to arrest through a kinematic hardening acceleration effect. A physics-informed neural network employing smooth Macaulay bracket approximation with curriculum learning reproduces all three regimes within a single trained surrogate. The framework is validated against experimental data using the creep-ageing and back-stress test (CABT), which provides independent measurements of inelastic strain and back-stress evolution.

Keywords: Threshold stress evolution, Back stress, Flow arrest, Kinematic hardening, Lyapunov stability, Physics-informed neural network

1. Introduction

Under sustained loading at elevated temperatures, the mechanical response of metallic materials is markedly time-dependent; classical elasticity and rate-independent plasticity are insufficient to describe such behaviour. When a metallic material is loaded, held under creep, and subsequently unloaded, the total strain separates into an instantaneous elastic recovery, a time-dependent reversible portion termed anelasticity, and a permanent viscous component that does not recover [1, 2]. Sinha [3, 4] was the first to investigate this separation systematically, through strain relaxation and recovery experiments on polycrystalline materials. For applications in which dimensional stability and springback prediction are required, an accurate constitutive description of the recoverable and irrecoverable components is indispensable.

The physical basis of anelasticity lies in internal stresses that oppose the applied stress during forward creep and subsequently drive strain recovery upon unloading. At the mesoscale, these internal stresses have been attributed to grain boundary shearing and sliding [5]; at the microscale, they are associated with the evolution of dislocation cell structures [6]. Mughrabi [7] proposed a composite model in which heterogeneous dislocation cells generate spatially varying stress fields — cell walls sustain stresses of the same sign as the applied load, while cell interiors carry stresses of opposite sign — so that the resulting stress heterogeneity furnishes the thermodynamic driving force for anelastic

Email address: y.yang@ntut.edu.tw (Yo-Lun Yang)

recovery. Zelenika et al. [8] recently obtained the first in-situ three-dimensional observations of approximately 40,000 dislocation cells during tensile deformation, using Dark Field X-ray Microscopy. Their measurements confirmed that cell size distributions are log-normal with bimodal dislocation density, lending quantitative support to composite models of the Mughrabi type. From a mechanistic standpoint, Li and Wagoner [9] proposed the Dissipative Bow-out model, which distinguishes three mechanisms underlying time-dependent recoverable strain, namely bond stretching (linear elastic), dislocation breakaway and multiplication (plastic), and dislocation bow-out (nonlinear elastic, dissipative).

At the macroscopic scale, these heterogeneous dislocation fields manifest as the back stress — defined as the volume-averaged internal stress opposing deformation — which occupies a central place in constitutive descriptions of anelastic behaviour [10, 11]. Zhu and Wu [12] introduced the hetero-deformation induced (HDI) stress framework, in which geometrically necessary dislocations (GNDs) pile up near zone boundaries, so that back stress develops in soft zones and forward stress in hard zones. Back stress may be measured by stress relaxation tests, incremental unloading procedures, or strain transient dip tests [13]; more recently, Chen et al. [14] proposed an HDI stress measurement method based on plastic dissipation in hysteresis loops, reporting higher accuracy than the classical Cottrell and Dickson approaches. In a broader assessment, Chen et al. [15] reviewed the coupling between dislocation substructure evolution and macroscopic mechanical response during high-temperature creep, and concluded that back stress is not merely a fitting parameter but reflects the evolving internal state of the material. Existing techniques, however, yield back-stress values only at discrete interruption points rather than during an ongoing creep process; the development of protocols capable of tracking back-stress evolution continuously therefore remains an open need.

In constitutive models, the onset of inelastic flow is determined by the applied stress, the back stress, and a threshold below which the macroscopic inelastic strain rate vanishes. Creep strain rate equations relate the deformation rate to stress, temperature, and internal state variables. The sinh-law formulation [16, 17] is generally preferred to simple power-law forms, since it reproduces both the low-stress linear regime and the high-stress power-law regime within a single expression. In threshold stress models, dislocation motion is assumed to require a critical stress to overcome obstacles — precipitates, grain boundaries, or forest dislocations — below which no macroscopic flow occurs.

Conventional viscoplasticity frameworks, following Perzyna [18] or Chaboche [19–21], treat the threshold stress as a material constant or as a function solely of accumulated plastic strain. When the microstructure remains stable during deformation, this treatment is adequate; it becomes unsuitable, however, when microstructural evolution — whether precipitation, phase transformation, solute clustering, or thermally-activated recovery — proceeds concurrently with creep. Meyer and Ahlström [22] showed that accumulated plastic strain alone does not suffice to describe yield surface evolution in pearlitic steel; additional state variables beyond accumulated strain are required. In aluminium alloys, Li et al. [23] observed double primary creep behaviour in AA2050-T34, attributed to simultaneous precipitate dissolution and nucleation. Ma et al. [24] developed stress-level-dependent models with bimodal precipitation that account for the resulting threshold stress evolution, and Wang et al. [25] formulated mechanism-based constitutive equations relating threshold stress to dislocation density. The phenomenon is not confined to aluminium alloys. Machado Alves da Fonseca et al. [26] documented how $\gamma'' \rightarrow \delta$ phase evolution during prolonged ageing at 700 °C alters the viscoplastic behaviour of Alloy 625, with creep rates changing by two orders of magnitude; their results indicate that time-dependent threshold evolution occurs across diverse alloy systems undergoing microstructural change.

Several unified constitutive models have been proposed to couple microstructural evolution with creep deformation. Li et al. [27] integrated nucleation, growth, and coarsening theories with dislocation-based creep mechanisms, so that microstructural evolution and macroscopic creep-ageing behaviour may be predicted concurrently under complex thermal and mechanical loading histories. Within a thermodynamic framework, Lei et al. [28] constructed a creep model incorporating vacancy diffusion, dislocation motion, grain boundary sliding, and void evolution, and reported predictions without empirical calibration. Bartošák and Horváth [29] extended the Chaboche framework to incorporate static recovery of kinematic hardening under creep-fatigue loading, coupling continuum damage mechanics with a unified viscoplastic model for cast iron; creep strains in their formulation arise from the static recovery term rather than from a separate creep law. These unified models have yielded useful predictions for the specific material systems to which they are applied; their formulations are, however, generally tied to particular alloy systems and loading conditions rather than derived from a general thermodynamic framework with evolving internal state variables.

Of the two internal variables that govern inelastic flow, the threshold stress determines whether flow occurs, and the back stress determines the direction and magnitude of that flow once it has been activated. Taken together,

these variables form the necessary basis of any viscoplastic model that seeks to represent the competition between time-driven and strain-driven hardening. Kinematic hardening provides the mathematical vehicle for back-stress evolution: it describes translation of the yield surface in stress space, and thereby furnishes the basis for representing the Bauschinger effect and related directional hardening phenomena [30, 31]. Alternative approaches to yield surface evolution, including rate-dependent phenomenological models [32] and two-surface formulations [33], describe hardening through geometric translation and expansion of the yield locus; the present work instead employs a single-surface formulation with time-dependent threshold evolution.

The kinematic hardening lineage adopted in the present work begins with Armstrong and Frederick [34], who introduced nonlinear kinematic hardening by incorporating a dynamic recovery term in the evolution of back stress; this term produces saturation under monotonic loading while permitting reversal during load path changes. Chaboche [35, 36] subsequently decomposed the back stress into multiple components; the Ohno–Wang models [37, 38] further modified the dynamic recovery formulation to obtain improved predictions of ratcheting behaviour. Ohno et al. [39] extended these evolution equations to include the effect of maximum plastic strain due to pre-loading and ratcheting, demonstrating that the interaction between isotropic and kinematic hardening governs the cyclic response under prior loading histories. Ning et al. [40] showed that standard Armstrong–Frederick rules are insufficient for anomalous multiaxial ratcheting in zirconium alloy tubes at elevated temperature, and proposed a general formulation that decouples asymmetry from initial yielding; their results expose the limitations of existing kinematic hardening rules under multiaxial loading.

Through physically-based crystal plasticity models, the connection between phenomenological back stress and the underlying dislocation microstructure has been placed on a quantitative footing. Zirkle et al. [41] derived back-stress evolution from dislocation substructure dynamics by treating the dislocation cell structure as a two-phase composite, in which back stress arises from plastic deformation incompatibility between hard (cell wall) and soft (cell interior) regions. Their analysis indicates that the nonlinearity in back-stress evolution originates in plastic deformation within wall phases rather than in phenomenological dynamic recovery terms. In a complementary approach, Evers et al. [42] formulated a nonlocal crystal plasticity model that accounts for dislocation–grain boundary interactions; their formulation distinguishes GND-induced isotropic hardening (forest hardening) from GND-induced kinematic hardening (back stress from inhomogeneous GND distribution). Zhang et al. [43] further quantified this distinction by developing a nonlocal crystal plasticity model for gradient-grained materials, in which kinematic hardening arises directly from GND pile-ups near grain boundaries; their simulations showed that small grains contribute disproportionately to GND-related back-stress development. Ispánovity et al. [44] showed that dipolar dislocation wall formation arises intrinsically from back-stress terms in continuum dislocation dynamics, thereby linking discrete and continuum descriptions of plasticity.

Decomposing back stress into physically distinct contributions sheds light on how time-driven and strain-driven mechanisms interact at the microstructural level. Qin et al. [45] proposed a hardening model combining isotropic, kinematic, and distortional contributions, in which a microstructure stress deviator retains loading history information; orthogonal loading is treated through yield surface distortion, while Bauschinger effects are described by kinematic hardening. Xu et al. [46] showed that decomposition of the back stress into intergranular and intragranular components allows strain-driven hardening (primarily intragranular development) to be distinguished from time-driven effects (intergranular relaxation and recovery) — a distinction that motivates the separate treatment of threshold stress and back-stress evolution adopted in the present work.

Any constitutive framework that incorporates evolving internal variables must satisfy thermodynamic admissibility. The internal state variable framework, rooted in the work of Coleman and Gurtin [47], furnishes the formal basis for constructing constitutive equations consistent with the Clausius–Duhem inequality. McDowell and Liu [48] recently extended this foundation through a hierarchical nonequilibrium thermodynamic treatment of thermally activated dislocation plasticity, establishing a formal Gibbs framework for internal state variable evolution laws that govern back stress and threshold stress in metals and alloys. McDowell [49] subsequently addressed the self-organisation of dislocation avalanches within the same nonequilibrium framework, showing that competing mechanisms — a jamming transition and a depinning transition — govern the emergence of scale-free intermittent flow; the competition between these mechanisms provides a physical analogy to the competitive hardening dynamics considered in the present work. Within this thermodynamic setting, Oppermann et al. [50] formulated a thermo-viscoplasticity model applicable over wide temperature ranges. Zhu et al. [51] derived a cyclic elasto-viscoplastic model from the Coleman–Noll procedure, incorporating Ohno–Abdel-Karim nonlinear kinematic hardening and validating the formulation

against cyclic deformation data at elevated temperature; their thermodynamic derivation parallels the approach employed in the present work. In a related development, Ren et al. [52] coupled damage evolution with nonlinear mixed kinematic hardening under multiaxial non-proportional loading, and showed that hysteresis loop shapes are predicted more accurately than by simpler models.

In creep-ageing conditions, where age-hardenable aluminium alloys undergo sustained mechanical loading and precipitation hardening simultaneously [53, 54], the competition between time-driven and strain-driven hardening is particularly pronounced. These conditions accordingly provide a well-characterised experimental basis for validating constitutive frameworks with evolving threshold stress. Wang et al. [55] modelled anisotropic creep-ageing behaviour of 2xxx aluminium alloys, employing non-uniform rational B-splines to extend rolling-direction material models to arbitrary loading orientations. Bignon et al. [56] developed a crystal plasticity model for dynamic precipitation in aluminium alloys that accounts for bidirectional coupling; in their formulation, the precipitate distribution affects the critical stress, while deformation accelerates precipitation kinetics — an interaction that illustrates the simultaneous operation of time-driven and strain-driven mechanisms.

Further evidence of this competition has emerged from studies of specific alloy systems. Ma et al. [24] formulated dislocation-based creep models with internal variables that account for upturn behaviour, in which creep strain and hardening response accelerate at high stress; their treatment incorporates bimodal precipitation involving shearable and non-shearable precipitate populations. Yang et al. [57] showed that superposed hardening from precipitates and dislocations governs the strength-ductility balance in Al–Cu alloys; their quantitative analysis indicated that fine θ' precipitates and pre-existing dislocations act in combination to enhance the mechanical response during ageing, providing direct experimental evidence of interaction between time-driven precipitation hardening and strain-driven effects. Li et al. [58] proposed a model for asymmetric tension and compression creep-ageing that predicts double primary creep with threshold creep stress and a microstructure-dependent creep variable; Zheng et al. [59] extended this class of model to multi-step creep-ageing, incorporating different precipitation kinetics at successive temperatures. Taken together, these studies confirm that the threshold stress cannot be treated as constant when microstructural evolution occurs concurrently with deformation [24, 25].

Despite the experimental evidence summarised above, existing creep models generally treat the threshold stress as either a constant material parameter or as a quantity evolving solely in response to accumulated strain [20]. Such a treatment neglects the time-dependent evolution of microstructural features — whether precipitates, second phases, or solute atmospheres — that govern flow resistance across a broad range of metallic materials. Moreover, the conditions under which inelastic flow ceases as the evolving threshold overtakes the effective stress — and whether such cessation is stable against perturbations — have not been formally analysed. Two distinct mechanisms contribute to threshold stress evolution and must be distinguished.

The first is the formation and dissipation of dislocation cell structures, a reversible process [8]. During primary creep, mobile dislocations pile up and form cell walls, and the resulting long-range internal stress fields oppose the applied stress. Upon unloading, these cell structures gradually dissipate, and anelastic recovery follows [60]. Because this process is reversible, it proceeds on timescales that are independent of the applied strain rate; it is common to all crystalline metals that form cellular dislocation arrangements.

The second is microstructural evolution that proceeds with physical time — precipitation hardening, phase transformation, and solute redistribution among its principal manifestations — and that contributes an irreversible component to threshold stress evolution [56, 61, 62]. In age-hardenable alloys, precipitates establish a stress floor below which thermally-activated dislocation bypass cannot occur; in other systems, analogous barriers arise from second-phase particles, solute atmospheres, or ordered domains. Unlike dislocation cell structures, these microstructure-induced contributions to flow resistance do not reverse upon unloading.

The coupling of these two mechanisms — reversible dislocation cell dynamics and irreversible microstructural evolution — produces hardening behaviour that conventional models do not predict. Experimental observations of anelastic recovery [4, 63], back-stress saturation during primary creep [11], and nonlinear stress dependence of creep rates in alloys undergoing concurrent microstructural change [23–25] together suggest the need for a constitutive framework in which the threshold stress is treated as an evolving state variable rather than a constant.

The present work addresses this need through a general framework derived from first principles — Clausius–Duhem thermodynamic consistency, Perzyna-type overstress viscoplasticity, and Armstrong–Frederick kinematic hardening — and not restricted to any particular alloy system or microstructural mechanism. In this framework, the threshold stress increases continuously with physical time (time-driven hardening), while back stress develops

only during active inelastic flow (strain-driven hardening); the interaction between these two mechanisms governs the resulting deformation behaviour.

On the basis of the relative magnitudes of the applied stress, the initial threshold, and the saturated threshold, three regimes of behaviour are identified, namely (I) a purely elastic response when the applied stress does not exceed the initial threshold; (II) flow arrest, in which inelastic flow initiates but subsequently ceases as microstructural strengthening raises the threshold above the local stress; and (III) continuous flow when the stress exceeds even the saturated threshold. Within the arrest regime, internal stress distributions become locked at the instant of cessation — a phenomenon termed stress freezing. A kinematic hardening acceleration effect is also predicted. Because back stress responds immediately to inelastic strain whereas threshold evolution proceeds gradually with physical time, the kinematic contribution provides early flow resistance that closes the gap before the threshold has fully developed, and the time to arrest is accordingly reduced.

The constitutive model developed in the present work involves a system of coupled ordinary differential equations (ODEs) whose parametric solution — mapping applied stress and time to inelastic strain and back stress — defines a continuous manifold across all three behavioural regimes. At individual parameter values, this manifold is readily obtained by direct numerical integration; the computation becomes prohibitive, however, when parametric sweeps or downstream structural analyses require repeated evaluation. Physics-informed neural networks (PINNs) provide a means of constructing continuous surrogate representations that embed the governing equations directly in the loss function [64–66]. Recent reviews by Dornheim et al. [67] and Fuhg et al. [68] treat the range of neural network approaches to constitutive modelling, from feedforward and recurrent to physics-informed architectures, together with verification methodologies for data-driven material laws. Jordan and Mohr [69] demonstrated that physics-based thermo-viscoplasticity models benefit from large-dataset training procedures, achieving accurate predictions of the large-deformation response of polypropylene across temperatures and strain rates spanning several orders of magnitude. The PINN methodology, introduced by Raissi et al. [70, 71], permits parameter identification from sparse experimental data while maintaining physical consistency.

Masi and Stefanou [72, 73] proposed the thermodynamics-based artificial neural network (TANN) framework, in which both laws of thermodynamics are encoded directly in the network architecture through automatic differentiation, providing a basis for thermodynamically consistent constitutive modelling. The Evolution TANN extension [73] allows data-driven identification of evolution equations and internal variables, with predictions that are independent of increment size. In the context of viscoplasticity, Eghtesad et al. [74] developed the NN-EVP framework for elasto-viscoplasticity, which accounts for grain size and strain rate sensitivity; monotonicity and convexity constraints are imposed to maintain thermodynamic consistency. Yu et al. [75] proposed a physics-informed multimodal network for unified prediction of ratcheting deformation at elevated temperatures, in which the unrecoverable character of plastic strain accumulation is incorporated directly in the loss function. Keshavarz et al. [76] integrated PINNs with crystal plasticity finite element methods within a large-deformation framework, and reported that the surrogate reproduces stress–strain responses and plastic deformation gradients at reduced computational cost. For finite-strain elasto-plasticity, Niu et al. [77] constructed a PINN framework that handles plastic deformation gradients and multi-step loading histories, and showed that the formulation extends to viscoplastic problems. Maia et al. [78] proposed physically recurrent neural networks that embed constitutive models within the network architecture; their formulation predicts unloading and reloading responses without explicit training data for these paths.

The non-smooth character of the elastic–inelastic transition, which in the present framework takes the form of a Macaulay bracket on the overstress, poses a particular difficulty for neural network training. Vlassis and Sun [79] addressed this by formulating yield functions as evolving level sets, with Hamilton–Jacobi equations governing hardening and softening. Lai et al. [80] introduced Locally Enhanced Neural Networks (LENNs), whose multiscale architecture separates the global bulk solution from localised non-smooth features by weighted superposition of smooth window functions.

For path-dependent plasticity, Gorji et al. [81] showed that recurrent neural networks based on gated recurrent units (GRUs), in which built-in memory variables represent plastic strains and back stresses, reproduce both the Bauschinger effect and latent hardening. Bonatti et al. [82] developed self-consistent recurrent neural network surrogates for crystal plasticity that provide stress responses independent of time-discretisation, making them suitable for integration into explicit finite element frameworks. Heidenreich and Mohr [83] extended this approach through the Extended Minimal State Cell (EMSC) architecture, which enforces stationarity and self-consistency for rate- and temperature-dependent viscoplastic constitutive modelling by mathematical construction — a stability requirement

analogous to the Lyapunov stability analysis presented in the present work. Danoun et al. [84] pursued a complementary strategy for non-proportional loading through stacked LSTM networks that satisfy thermodynamic consistency, with physics-based loss functions enforcing dissipation compliance.

Although physics-informed neural networks have been applied to rate-independent plasticity [85] and thermo-viscoplasticity [86], no existing formulation addresses the situation in which the threshold evolves independently of accumulated strain while competing with strain-driven back-stress evolution.

The present work contributes the following. A constitutive framework is formulated in which the threshold stress evolves autonomously with physical time through microstructural kinetics, independently of accumulated strain — a departure from conventional viscoplasticity in which the threshold is either constant or strain-driven. Modified Armstrong–Frederick kinematic hardening with static recovery is incorporated, and the interaction between time-driven threshold evolution and strain-driven back stress is shown to produce three distinct behavioural regimes. Flow arrest — in which inelastic flow initiates but subsequently ceases — is proven to be asymptotically stable via a constructive Lyapunov function, the first such stability proof at the material-point level in the viscoplastic creep literature. A kinematic hardening acceleration effect is derived, showing that back-stress development reduces the time to arrest. A physics-informed neural network employing smooth Macaulay bracket approximation with curriculum learning reproduces all three behavioural regimes within a single trained network. The framework is validated on AA7050-T6 aluminium alloy at 174 °C — a system in which precipitation-driven threshold evolution is particularly pronounced — using the creep-ageing and back-stress test (CABT), a measurement technique developed by the present author [87]. The loading phase of the CABT provides time-resolved inelastic strain histories, while the post-unloading phase yields direct back-stress measurements, so that both subsystems are validated independently. The CABT protocol and the related creep-ageing recovery test (CART) are illustrated in Figure 1, which presents the experimental approaches for measuring inelastic strain and back-stress evolution.

2. Constitutive Framework

2.1. Thermodynamic Foundation

For a viscoplastic material exhibiting both recoverable and permanent inelastic deformation, the constitutive framework is developed within the thermodynamics of internal variables, following the internal state variable approach of Coleman and Gurtin [47]. The observable state is specified by the total strain tensor $\boldsymbol{\varepsilon}$ and the temperature T, assumed constant throughout. In addition to these observable quantities, it is necessary to introduce two internal state variables. Of these, the anelastic strain tensor $\boldsymbol{\varepsilon}^{\mathrm{an}}$ is associated with recoverable time-dependent deformation, while the scalar ageing variable ξ describes the degree of microstructural strengthening.

Under the assumption of small strains, the total strain decomposes additively, so that

$$\boldsymbol{\varepsilon} = \boldsymbol{\varepsilon}^{\mathrm{e}} + \boldsymbol{\varepsilon}^{\mathrm{in}} \tag{1}$$

where $\boldsymbol{\varepsilon}^{\mathrm{e}}$ is the elastic strain and $\boldsymbol{\varepsilon}^{\mathrm{in}}$ the inelastic strain. The inelastic strain is itself partitioned into recoverable and permanent parts,

$$\boldsymbol{\varepsilon}^{\mathrm{in}} = \boldsymbol{\varepsilon}^{\mathrm{an}} + \boldsymbol{\varepsilon}^{\mathrm{vis}} \tag{2}$$

The anelastic component $\boldsymbol{\varepsilon}^{\mathrm{an}}$ is associated with heterogeneous dislocation cell structures whose internal stress fields store elastic energy; upon unloading, this stored energy furnishes the driving force for strain recovery. In contrast, the viscous component $\boldsymbol{\varepsilon}^{\mathrm{vis}}$ arises from dislocation climb and annihilation, and is not recovered.

The specific Helmholtz free energy ψ is taken as the sum of elastic, anelastic, and microstructural contributions,

$$\psi = \psi^{\mathrm{e}}\left(\boldsymbol{\varepsilon}^{\mathrm{e}}\right) + \psi^{\mathrm{an}}\left(\boldsymbol{\varepsilon}^{\mathrm{an}}\right) + \psi^{\mathrm{age}}(\xi) \tag{3}$$

where $\xi \in [0, 1]$ is the dimensionless ageing variable. For isotropic linear elasticity, the elastic free energy is

$$\psi^{\mathrm{e}} = \frac{1}{2\rho}\boldsymbol{\varepsilon}^{\mathrm{e}} : \mathbb{C} : \boldsymbol{\varepsilon}^{\mathrm{e}} = \frac{1}{2\rho}\left[\lambda\left(\operatorname{tr}\boldsymbol{\varepsilon}^{\mathrm{e}}\right)^2 + 2\mu\,\boldsymbol{\varepsilon}^{\mathrm{e}} : \boldsymbol{\varepsilon}^{\mathrm{e}}\right] \tag{4}$$

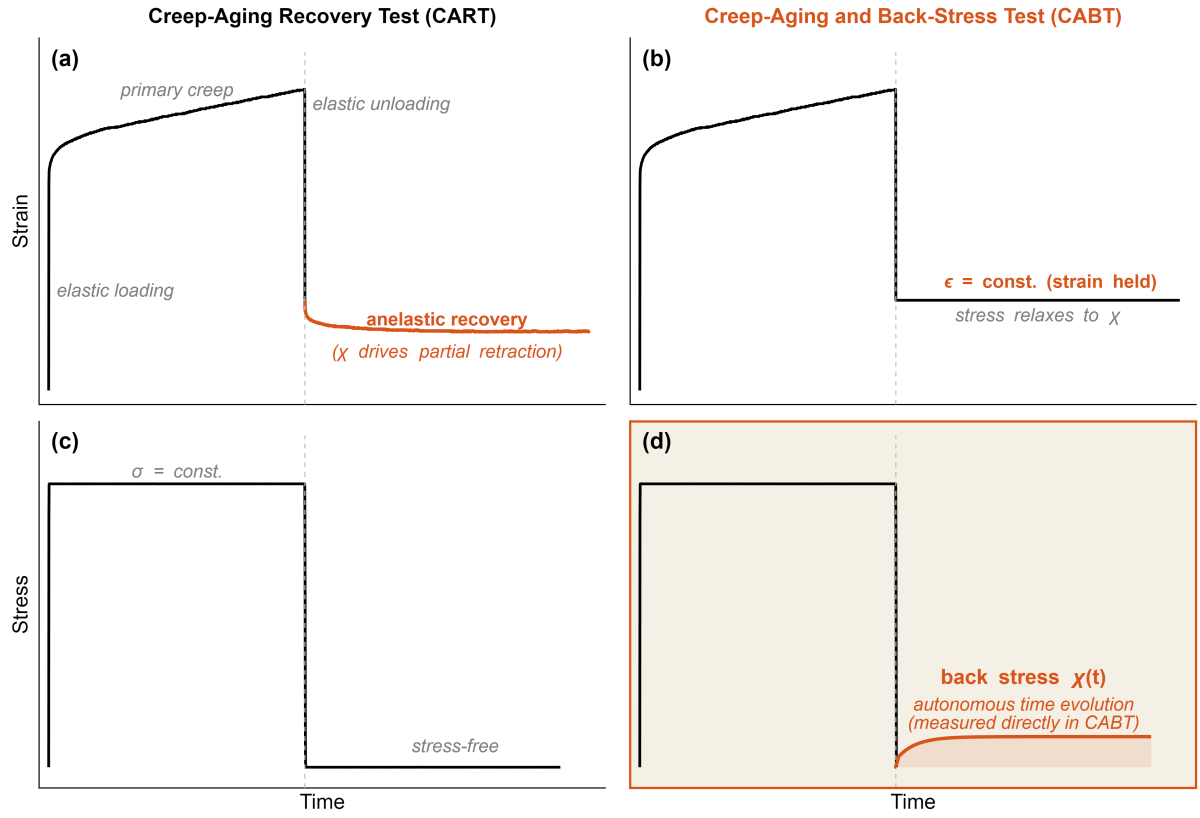

Figure 1: Schematic comparison of the creep-ageing recovery test (CART) and the creep-ageing and back-stress test (CABT); the two protocols measure inelastic strain and back-stress evolution respectively. (a) Strain response in CART: primary creep followed by anelastic recovery upon unloading; the back stress χ drives partial retraction. (b) Strain response in CABT: strain held constant after unloading; stress relaxes to χ. (c) Stress protocol for CART: constant applied stress followed by stress-free recovery. (d) Stress protocol for CABT: constant applied stress followed by strain-constrained hold, from which the autonomous back stress $\chi(t)$ is obtained.

where ρ is the mass density, $\mathbb{C}$ the fourth-order elasticity tensor, and λ and μ the Lamé constants. The energy stored in dislocation cell wall stress fields takes the quadratic form

$$\psi^{\mathrm{an}} = \frac{c}{2\rho}\boldsymbol{\varepsilon}^{\mathrm{an}} : \boldsymbol{\varepsilon}^{\mathrm{an}} \tag{5}$$

with c [MPa] denoting the kinematic hardening modulus, which may be regarded as a measure of the stiffness of the internal dislocation structure. The contribution from microstructural ageing — associated with precipitate–matrix interfacial energy and coherency strains — may be written as

$$\psi^{\mathrm{age}} = \frac{H_\xi}{2\rho}(\xi - 1)^2 \tag{6}$$

where H_ξ [MPa] is the microstructural hardening modulus. The function ψ^{age} attains its minimum at $\xi = 1$, corresponding to the fully aged condition at thermodynamic equilibrium.

Under isothermal conditions, the requirement of non-negative dissipation is expressed by the Clausius–Duhem inequality,

$$\mathcal{D} = \boldsymbol{\sigma} : \dot{\boldsymbol{\varepsilon}} - \rho\dot{\psi} \geq 0 \tag{7}$$

Here $\boldsymbol{\sigma}$ is the Cauchy stress tensor and the superposed dot denotes the material time derivative. Expanding the free energy rate gives

$$\rho\dot{\psi} = \rho\frac{\partial\psi}{\partial\boldsymbol{\varepsilon}^{\mathrm{e}}} : \dot{\boldsymbol{\varepsilon}}^{\mathrm{e}} + \rho\frac{\partial\psi}{\partial\boldsymbol{\varepsilon}^{\mathrm{an}}} : \dot{\boldsymbol{\varepsilon}}^{\mathrm{an}} + \rho\frac{\partial\psi}{\partial\xi}\dot{\xi} \tag{8}$$

Substituting into (7) with $\dot{\boldsymbol{\varepsilon}} = \dot{\boldsymbol{\varepsilon}}^{\mathrm{e}} + \dot{\boldsymbol{\varepsilon}}^{\mathrm{in}}$, and rearranging, we obtain

$$\mathcal{D} = \left(\boldsymbol{\sigma} - \rho\frac{\partial\psi}{\partial\boldsymbol{\varepsilon}^{\mathrm{e}}}\right) : \dot{\boldsymbol{\varepsilon}}^{\mathrm{e}} + \boldsymbol{\sigma} : \dot{\boldsymbol{\varepsilon}}^{\mathrm{in}} - \rho\frac{\partial\psi}{\partial\boldsymbol{\varepsilon}^{\mathrm{an}}} : \dot{\boldsymbol{\varepsilon}}^{\mathrm{an}} - \rho\frac{\partial\psi}{\partial\xi}\dot{\xi} \geq 0 \tag{9}$$

Since this inequality must hold for arbitrary elastic strain rates, the coefficient of $\dot{\boldsymbol{\varepsilon}}^{\mathrm{e}}$ must vanish identically, giving the elastic constitutive relation

$$\boldsymbol{\sigma} = \rho\frac{\partial\psi}{\partial\boldsymbol{\varepsilon}^{\mathrm{e}}} = \mathbb{C} : \left(\boldsymbol{\varepsilon} - \boldsymbol{\varepsilon}^{\mathrm{in}}\right) \tag{10}$$

The thermodynamic force conjugate to the anelastic strain defines the back-stress tensor,

$$\boldsymbol{\chi} = \rho\frac{\partial\psi}{\partial\boldsymbol{\varepsilon}^{\mathrm{an}}} = c\,\boldsymbol{\varepsilon}^{\mathrm{an}} \tag{11}$$

which may be interpreted physically as the internal stress generated by mobile dislocation structures; it opposes the applied stress and so reduces the effective driving force for continued flow. Similarly, the thermodynamic force conjugate to the ageing variable furnishes

$$Y_\xi = -\rho\frac{\partial\psi}{\partial\xi} = -H_\xi(\xi - 1) = H_\xi(1 - \xi) \tag{12}$$

The conjugate force Y_ξ is non-negative for $\xi \in [0, 1]$ and vanishes at equilibrium ($\xi = 1$). Substituting (10), (11), and (12) into (9), the reduced dissipation inequality becomes

$$\mathcal{D} = (\boldsymbol{\sigma} - \boldsymbol{\chi}) : \dot{\boldsymbol{\varepsilon}}^{\mathrm{an}} + \boldsymbol{\sigma} : \dot{\boldsymbol{\varepsilon}}^{\mathrm{vis}} + Y_\xi\dot{\xi} \geq 0 \tag{13}$$

and all admissible evolution equations are required to satisfy this inequality.

2.2. Flow Rule and Threshold Evolution

The effective stress driving inelastic flow is obtained by subtracting the back stress from the deviatoric stress, giving

$$\boldsymbol{\Sigma} = \boldsymbol{\sigma}' - \boldsymbol{\chi} \tag{14}$$

where $\boldsymbol{\sigma}' = \boldsymbol{\sigma} - (1/3)\,(\mathrm{tr}\,\boldsymbol{\sigma})\,\mathbf{I}$ is the deviatoric stress and $\mathbf{I}$ the second-order identity tensor. Since inelastic flow is incompressible ($\mathrm{tr}\,\dot{\boldsymbol{\varepsilon}}^{\mathrm{in}} = 0$), the back stress is purely deviatoric. The von Mises equivalent of the effective stress is

$$\Sigma_{\mathrm{eq}} = \sqrt{\frac{3}{2}\boldsymbol{\Sigma} : \boldsymbol{\Sigma}} \tag{15}$$

A yield function with time-dependent threshold is introduced as

$$f\,(\boldsymbol{\Sigma}, \sigma_Y) = \Sigma_{\mathrm{eq}} - \sigma_Y(\xi) \tag{16}$$

In contrast to classical formulations, in which the threshold is taken as constant or as a function of accumulated strain, here σ_Y evolves with time through the ageing variable ξ, giving

$$\sigma_Y(\xi) = \sigma_{Y0} + \Delta\sigma_Y \cdot \xi \tag{17}$$

where σ_{Y0} [MPa] is the initial threshold and $\Delta\sigma_Y$ [MPa] the threshold increment.

The ageing kinetics are assumed to follow first-order evolution,

$$\dot{\xi} = \frac{1}{\tau_h}(1 - \xi) \tag{18}$$

where τ_h [s] is the hardening time constant. Integration of (18) gives the exponential form

$$\xi(t) = 1 - e^{-t/\tau_h} \tag{19}$$

and substituting (19) into (17) yields

$$\sigma_Y(t) = \sigma_{Y0} + \Delta\sigma_Y \left(1 - e^{-t/\tau_h}\right) \tag{20}$$

The equivalent rate form is

$$\dot{\sigma}_Y = \frac{1}{\tau_h}\,(\sigma_{Y\infty} - \sigma_Y) \tag{21}$$

where $\sigma_{Y\infty} = \sigma_{Y0} + \Delta\sigma_Y$ is the saturation threshold. It is this autonomous evolution that distinguishes the present formulation from conventional viscoplasticity: the threshold stress σ_Y increases with physical time regardless of whether flow is occurring, while the back stress $\boldsymbol{\chi}$ develops only during active inelastic deformation.

For associative viscoplasticity, the flow direction is taken normal to the yield surface, so that

$$\mathbf{N} = \frac{\partial f}{\partial \boldsymbol{\sigma}} \tag{22}$$

Applying the chain rule through the effective stress, we have

$$\frac{\partial f}{\partial \boldsymbol{\sigma}} = \frac{\partial f}{\partial \boldsymbol{\Sigma}} : \frac{\partial \boldsymbol{\Sigma}}{\partial \boldsymbol{\sigma}} = \frac{3}{2}\frac{\boldsymbol{\Sigma}}{\Sigma_{\mathrm{eq}}} : \mathbb{D} \tag{23}$$

where $\mathbb{D}$ is the fourth-order deviatoric projection tensor. Since $\boldsymbol{\Sigma}$ is already deviatoric, the expression reduces to

$$\mathbf{N} = \frac{3}{2}\frac{\boldsymbol{\Sigma}}{\Sigma_{\mathrm{eq}}} \tag{24}$$

with the normalisation $\mathbf{N} : \mathbf{N} = 3/2$. The inelastic strain rate takes the form

$$\dot{\boldsymbol{\varepsilon}}^{\mathrm{in}} = \dot{p}\,\mathbf{N} \tag{25}$$

where the equivalent inelastic strain rate follows a power-law overstress relation,

$$\dot{p} = \frac{1}{\eta} \left\langle \frac{\Sigma_{\mathrm{eq}} - \sigma_Y(\xi)}{\sigma_0} \right\rangle^n \tag{26}$$

Here η [s] is the viscosity parameter, σ_0 [MPa] a reference stress, n the stress exponent, and $\langle\cdot\rangle$ the Macaulay bracket defined by

$$\langle x \rangle = \frac{x + |x|}{2} = \max(0, x) \tag{27}$$

The power-law overstress formulation is adopted here for analytical tractability; the sinh-law variant [16, 17], which reproduces both low-stress linear and high-stress power-law behaviour within a single expression, may be substituted without affecting the thermodynamic structure or the regime classification developed in Section 3.

Combining (24), (25), and (26), the complete flow rule becomes

$$\dot{\boldsymbol{\varepsilon}}^{\mathrm{in}} = \frac{1}{\eta} \left\langle \frac{\Sigma_{\mathrm{eq}} - \sigma_Y(\xi)}{\sigma_0} \right\rangle^n \frac{3}{2} \frac{\boldsymbol{\Sigma}}{\Sigma_{\mathrm{eq}}} \tag{28}$$

The equivalent strain rate may also be written as

$$\dot{p} = \sqrt{\frac{2}{3} \dot{\boldsymbol{\varepsilon}}^{\mathrm{in}} : \dot{\boldsymbol{\varepsilon}}^{\mathrm{in}}} \tag{29}$$

as is readily verified by substituting (25) and using (24).

2.3. Back Stress Evolution with Static Recovery

The back stress is governed by a modified Armstrong–Frederick evolution equation with an additional static recovery term,

$$\dot{\boldsymbol{\chi}} = c\, \dot{\boldsymbol{\varepsilon}}^{\mathrm{in}} - \varkappa \boldsymbol{\chi}\, \dot{p} - \frac{\boldsymbol{\chi}}{\tau_{\mathrm{rec}}} \tag{30}$$

where $\varkappa$ is the dimensionless dynamic recovery coefficient and τ_{rec} [s] the static recovery time constant. On the right-hand side, the first term accounts for dislocation structure buildup during flow, the second for dynamic recovery through strain-induced annihilation, and the third for static recovery by thermal relaxation. Of these, the first two are active only during inelastic flow ($\dot{p} > 0$), whereas the static recovery term operates continuously, even in the absence of external loading. It is this last term that distinguishes the present evolution equation from the classical Armstrong–Frederick form; it represents thermally activated processes such as dislocation climb and cell coarsening.

The form of (30) may be motivated by a rheological model consisting of an internal Maxwell element through which the inelastic strain passes. The internal spring, of stiffness c, stores energy and generates back stress according to

$$\boldsymbol{\chi} = c\, \boldsymbol{\varepsilon}^{\mathrm{an}} \tag{31}$$

while the internal dashpot, of viscosity η_{int}, permits viscous relaxation,

$$\dot{\boldsymbol{\varepsilon}}_{\mathrm{int}}^{\mathrm{vis}} = \frac{\boldsymbol{\chi}}{\eta_{\mathrm{int}}} \tag{32}$$

Defining $\tau_{\mathrm{rec}} = \eta_{\mathrm{int}}/c$ and incorporating dynamic recovery during active flow, we recover equation (30). The parameter τ_{rec} accordingly has a direct physical interpretation as the characteristic timescale over which back stress relaxes under zero external loading; the rheological arrangement is illustrated in Figure 2.

Under multiaxial loading, the directional dependence of back-stress accumulation produces anisotropic recovery, in which directions with larger accumulated back stress recover more than those with less. The peak deformed and recovered strain states on the unit sphere under prescribed triaxial stress are shown in Figure 3.

Under constant strain rate proportional loading, the back stress approaches a steady-state value; in creep under constant stress, $\dot{p}$ varies with time, but the saturation value (34) corresponds to the instantaneous equilibrium toward which χ tends at the prevailing strain rate. Setting $\dot{\boldsymbol{\chi}} = \mathbf{0}$ in (30) gives

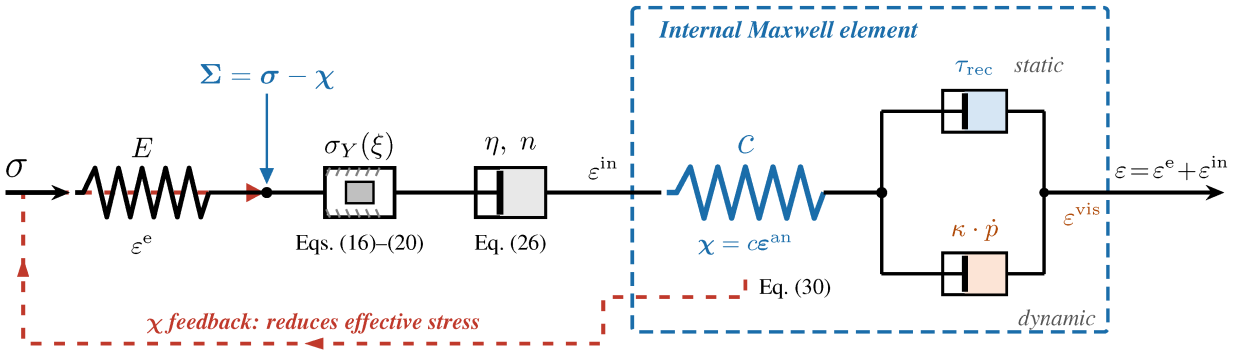

Figure 2: Rheological representation of the constitutive framework: elastic spring (E), ageing-dependent threshold element $\sigma_Y(\xi)$, viscoplastic dashpot (η, n), and internal Maxwell element for kinematic hardening with static (τ_{rec}) and dynamic ($\varkappa \cdot \dot{p}$) recovery mechanisms. The effective stress $\Sigma = \sigma - \chi$ drives flow through the threshold.

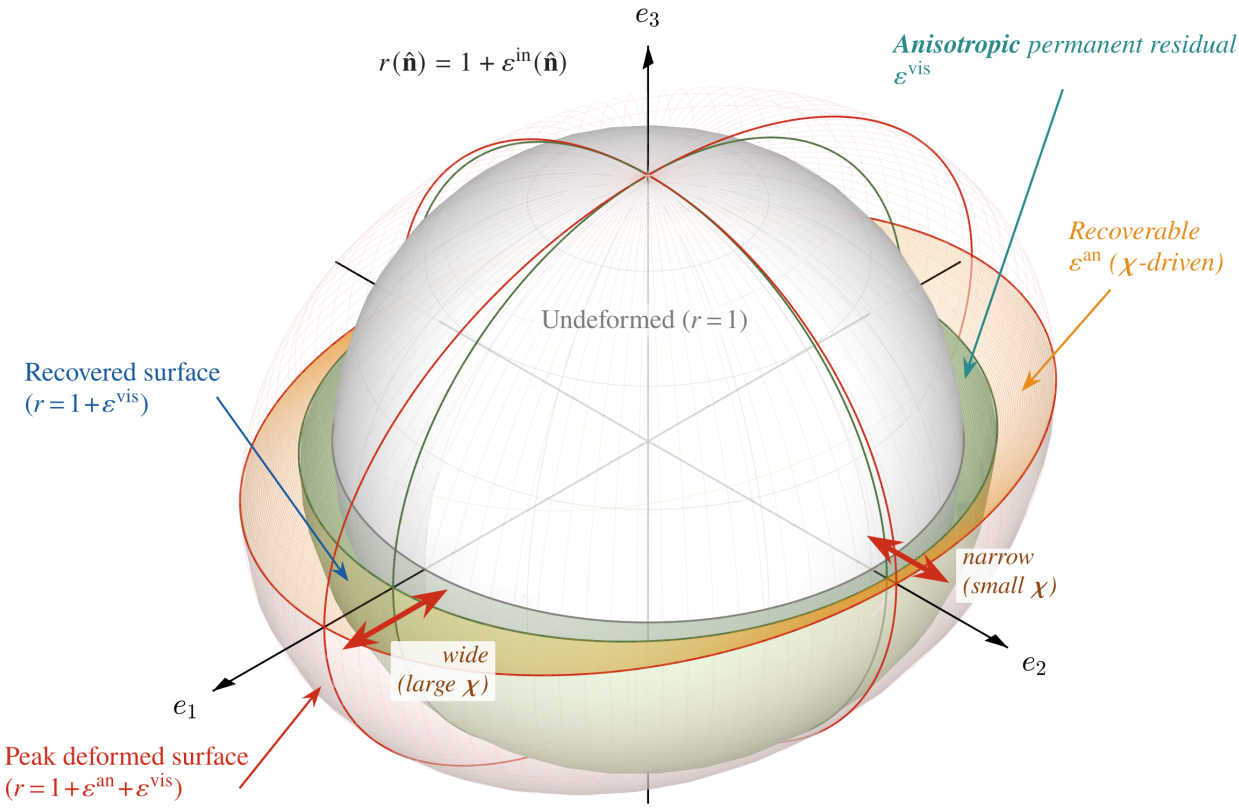

Figure 3: Anisotropic inelastic strain decomposition visualised on the unit sphere. The peak deformed surface (red) and recovered surface (green) are obtained by integrating the flow rule (28) and back-stress evolution (30) under prescribed triaxial stress ($\sigma_1 > \sigma_2 > \sigma_3$). Directions with larger accumulated back stress recover more, producing an irregular residual shape distinct from the deformed shape. Parameters chosen for visual clarity.

$$0 = c\,\dot{p} - \varkappa \chi_{\mathrm{sat}} \dot{p} - \frac{\chi_{\mathrm{sat}}}{\tau_{\mathrm{rec}}} \tag{33}$$

and solving for χ_{sat}, we obtain

$$\chi_{\mathrm{sat}} = \frac{c\,\dot{p}}{\varkappa \dot{p} + 1/\tau_{\mathrm{rec}}} = \frac{c}{\varkappa + 1/(\dot{p}\tau_{\mathrm{rec}})} \tag{34}$$

It follows from (34) that the saturation value depends on the strain rate solely through the dimensionless group $\dot{p}\tau_{\mathrm{rec}}$. When loading is fast ($\dot{p}\tau_{\mathrm{rec}} \gg 1$), dynamic recovery dominates and $\chi_{\mathrm{sat}} \to c/\varkappa$; when loading is slow ($\dot{p}\tau_{\mathrm{rec}} \ll 1$), static recovery dominates and $\chi_{\mathrm{sat}} \to c\,\dot{p}\,\tau_{\mathrm{rec}}$. The crossover between these two regimes occurs at the characteristic rate $\dot{p}^* = 1/(\varkappa\tau_{\mathrm{rec}})$; the saturation behaviour therefore spans continuously from the rate-independent limit to the fully viscous limit. Figure 4 shows $\chi_{\mathrm{sat}}/(c/\varkappa)$ as a function of the dimensionless group $\dot{p}\tau_{\mathrm{rec}}$.

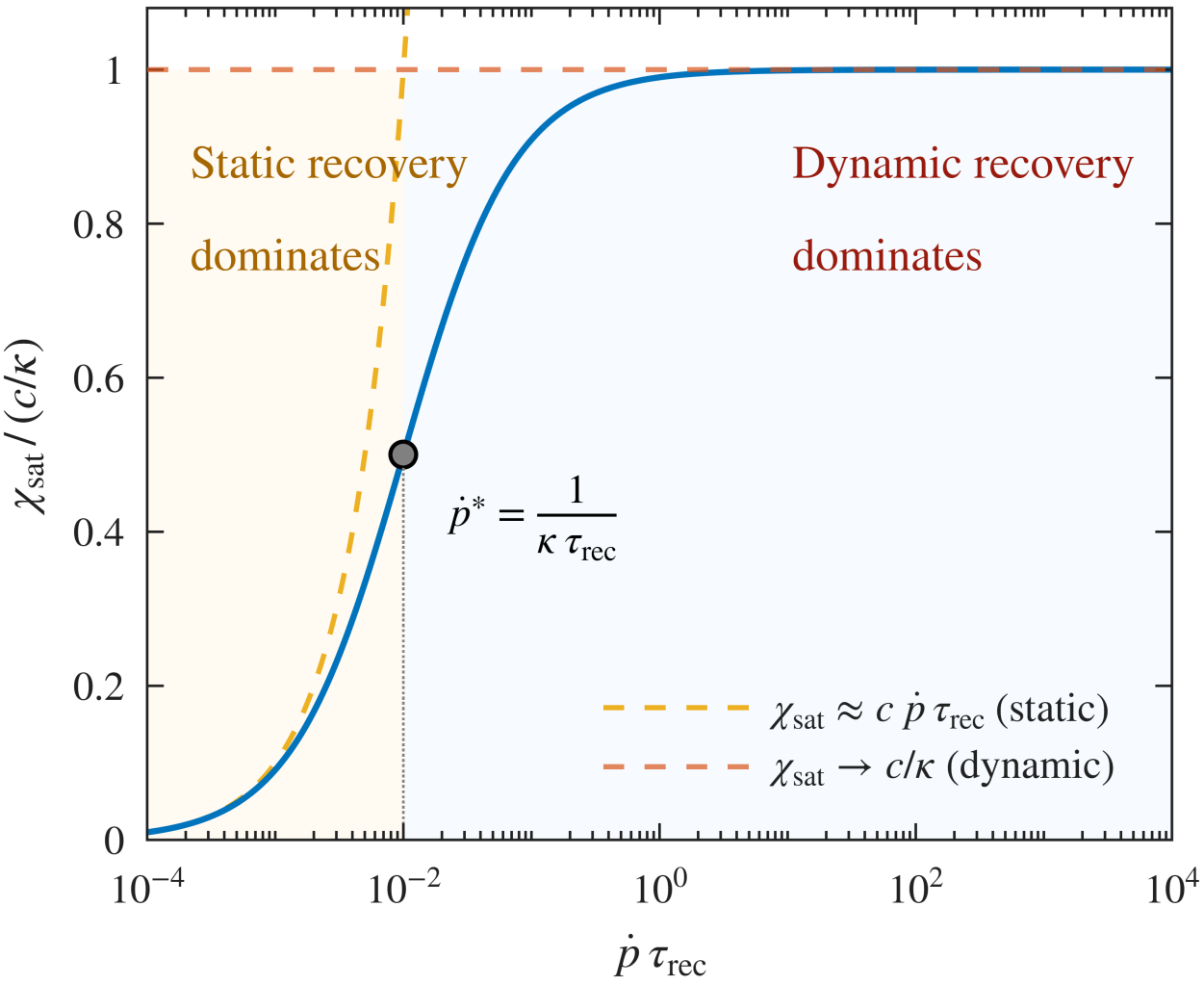

Figure 4: Normalised back-stress saturation $\chi_{\mathrm{sat}}/(c/\varkappa)$ as a function of the dimensionless strain rate–recovery time product $\dot{p}\tau_{\mathrm{rec}}$, showing the transition from static-recovery-dominated ($\chi_{\mathrm{sat}} \approx c\dot{p}\tau_{\mathrm{rec}}$) to dynamic-recovery-dominated ($\chi_{\mathrm{sat}} \to c/\varkappa$) regimes. The crossover occurs at $\dot{p}^* = 1/(\varkappa\tau_{\mathrm{rec}})$.

The partition of the inelastic strain rate into anelastic and viscous parts follows from (31) and (30). Differentiating (31) with respect to time gives

$$\dot{\boldsymbol{\chi}} = c\,\dot{\boldsymbol{\varepsilon}}^{\mathrm{an}} \tag{35}$$

and substituting the back-stress evolution equation, we obtain the anelastic strain rate as

$$\dot{\boldsymbol{\varepsilon}}^{\mathrm{an}} = \frac{1}{c}\dot{\boldsymbol{\chi}} = \dot{\boldsymbol{\varepsilon}}^{\mathrm{in}} - \frac{\varkappa}{c}\boldsymbol{\chi}\,\dot{p} - \frac{\boldsymbol{\chi}}{c\,\tau_{\mathrm{rec}}} \tag{36}$$

Since $\dot{\boldsymbol{\varepsilon}}^{\mathrm{in}} = \dot{\boldsymbol{\varepsilon}}^{\mathrm{an}} + \dot{\boldsymbol{\varepsilon}}^{\mathrm{vis}}$, it follows that the viscous strain rate is

$$\dot{\boldsymbol{\varepsilon}}^{\mathrm{vis}} = \frac{\varkappa}{c}\boldsymbol{\chi}\,\dot{p} + \frac{\boldsymbol{\chi}}{c\,\tau_{\mathrm{rec}}} \tag{37}$$

The viscous strain accordingly accumulates through two mechanisms, namely dynamic conversion during active flow and static conversion by thermal relaxation.

When the stress lies below the threshold ($\Sigma_{\mathrm{eq}} < \sigma_Y$), the Macaulay bracket gives $\dot{p} = 0$ and the evolution equations reduce to

$$\dot{\boldsymbol{\chi}} = -\frac{\boldsymbol{\chi}}{\tau_{\mathrm{rec}}}, \quad \dot{\boldsymbol{\varepsilon}}^{\mathrm{an}} = -\frac{\boldsymbol{\chi}}{c\,\tau_{\mathrm{rec}}}, \quad \dot{\boldsymbol{\varepsilon}}^{\mathrm{vis}} = \frac{\boldsymbol{\chi}}{c\,\tau_{\mathrm{rec}}} \tag{38}$$

which integrate to

$$\boldsymbol{\chi}(t) = \boldsymbol{\chi}_0\, e^{-t/\tau_{\mathrm{rec}}}, \quad \boldsymbol{\varepsilon}^{\mathrm{an}}(t) = \boldsymbol{\varepsilon}^{\mathrm{an}}_0\, e^{-t/\tau_{\mathrm{rec}}} \tag{39}$$

The anelastic strain therefore decays exponentially towards zero while the viscous strain accumulates the permanent component. This exponential recovery is the mechanism responsible for the creep recovery observed experimentally in strain relaxation and recovery tests [3, 4].

2.4. Thermodynamic Consistency

The constitutive model defined by Eqs. (28), (30), (36), (37), and (18) satisfies the Clausius–Duhem inequality for all admissible processes. Starting from the reduced dissipation (13), and noting that $\dot{\boldsymbol{\varepsilon}}^{\mathrm{an}}$ and $\dot{\boldsymbol{\varepsilon}}^{\mathrm{vis}}$ are traceless, the dissipation may be expressed in terms of deviatoric quantities as

$$\mathcal{D} = \boldsymbol{\Sigma} : \dot{\boldsymbol{\varepsilon}}^{\mathrm{an}} + \boldsymbol{\sigma}' : \dot{\boldsymbol{\varepsilon}}^{\mathrm{vis}} + Y_{\xi}\dot{\xi} \tag{40}$$

Substituting the anelastic strain rate from (36) gives

$$\boldsymbol{\Sigma} : \dot{\boldsymbol{\varepsilon}}^{\mathrm{an}} = \boldsymbol{\Sigma} : \dot{\boldsymbol{\varepsilon}}^{\mathrm{in}} - \frac{\varkappa}{c}\,(\boldsymbol{\Sigma} : \boldsymbol{\chi})\,\dot{p} - \frac{(\boldsymbol{\Sigma} : \boldsymbol{\chi})}{c\,\tau_{\mathrm{rec}}} \tag{41}$$

On introducing the flow rule $\dot{\boldsymbol{\varepsilon}}^{\mathrm{in}} = \dot{p}\,\mathbf{N}$ and $\mathbf{N} = (3/2)\boldsymbol{\Sigma}/\Sigma_{\mathrm{eq}}$, the first term on the right-hand side becomes

$$\boldsymbol{\Sigma} : \dot{\boldsymbol{\varepsilon}}^{\mathrm{in}} = \dot{p}\,\boldsymbol{\Sigma} : \frac{3}{2}\frac{\boldsymbol{\Sigma}}{\Sigma_{\mathrm{eq}}} = \frac{3\dot{p}}{2\Sigma_{\mathrm{eq}}}\,(\boldsymbol{\Sigma} : \boldsymbol{\Sigma}) = \Sigma_{\mathrm{eq}}\,\dot{p} \tag{42}$$

where we have used $\boldsymbol{\Sigma} : \boldsymbol{\Sigma} = (2/3)\Sigma_{\mathrm{eq}}^2$. Substituting the viscous strain rate from (37) in a similar manner yields

$$\boldsymbol{\sigma}' : \dot{\boldsymbol{\varepsilon}}^{\mathrm{vis}} = \frac{\varkappa}{c}\,(\boldsymbol{\sigma}' : \boldsymbol{\chi})\,\dot{p} + \frac{(\boldsymbol{\sigma}' : \boldsymbol{\chi})}{c\,\tau_{\mathrm{rec}}} \tag{43}$$

Since $\boldsymbol{\sigma}' - \boldsymbol{\Sigma} = \boldsymbol{\chi}$, we have

$$\boldsymbol{\sigma}' : \boldsymbol{\chi} - \boldsymbol{\Sigma} : \boldsymbol{\chi} = \boldsymbol{\chi} : \boldsymbol{\chi} = \|\boldsymbol{\chi}\|^2 \tag{44}$$

where $\|\boldsymbol{\chi}\|^2 = \boldsymbol{\chi} : \boldsymbol{\chi}$ is the squared Frobenius norm. Collecting terms from (41)–(44), the mechanical dissipation simplifies to

$$\mathcal{D}_{\mathrm{mech}} = \Sigma_{\mathrm{eq}}\,\dot{p} + \frac{\varkappa}{c}\|\boldsymbol{\chi}\|^2\dot{p} + \frac{\|\boldsymbol{\chi}\|^2}{c\,\tau_{\mathrm{rec}}} \tag{45}$$

Each term on the right-hand side is non-negative, since $\Sigma_{\mathrm{eq}} \geq 0$ by definition, $\dot{p} \geq 0$ from the Macaulay bracket, $\varkappa$, c, $\tau_{\mathrm{rec}} > 0$ as material parameters, and $\|\boldsymbol{\chi}\|^2 \geq 0$. It follows that

$$\mathcal{D}_{\mathrm{mech}} \geq 0 \quad \text{for all admissible processes} \tag{46}$$

The total dissipation may be decomposed into four contributions,

$$\mathcal{D}_{\mathrm{total}} = \mathcal{D}_{\mathrm{flow}} + \mathcal{D}_{\mathrm{dyn}} + \mathcal{D}_{\mathrm{stat}} + \mathcal{D}_{\mathrm{age}} \tag{47}$$

in which $\mathcal{D}_{\mathrm{flow}} = \Sigma_{\mathrm{eq}}\,\dot{p}$ is the viscous resistance to inelastic flow, $\mathcal{D}_{\mathrm{dyn}} = (\varkappa/c)\|\boldsymbol{\chi}\|^2\dot{p}$ the dissipation associated with dynamic recovery, $\mathcal{D}_{\mathrm{stat}} = \|\boldsymbol{\chi}\|^2/(c\,\tau_{\mathrm{rec}})$ the static recovery dissipation, and $\mathcal{D}_{\mathrm{age}} = Y_\xi\dot{\xi}$ the contribution from microstructural ageing. Of these four terms, $\mathcal{D}_{\mathrm{stat}}$ is of particular interest: it remains positive whenever $\boldsymbol{\chi} \neq \mathbf{0}$, regardless of whether inelastic flow is occurring, so that energy is dissipated by thermal relaxation of dislocation structures even in the absence of mechanical loading. Classical kinematic hardening models, which lack a static recovery mechanism, do not exhibit this behaviour.

The thermodynamic treatment of the threshold stress $\sigma_Y(t)$ deserves separate comment. Unlike the back stress — which evolves only during active flow — the threshold increases continuously with time irrespective of the mechanical loading state; this time-driven evolution is accommodated through the internal ageing variable ξ introduced in Section 2.1. The microstructural dissipation associated with ageing is non-negative,

$$\mathcal{D}_{\mathrm{age}} = Y_\xi\dot{\xi} \geq 0 \tag{48}$$

Substituting the thermodynamic force (12) and the ageing kinetics (18) gives

$$\mathcal{D}_{\mathrm{age}} = H_\xi(1-\xi)\cdot\frac{1}{\tau_h}(1-\xi) = \frac{H_\xi}{\tau_h}(1-\xi)^2 \geq 0 \tag{49}$$

The inequality is strict for $\xi < 1$ and vanishes at equilibrium ($\xi = 1$). The total dissipation therefore satisfies

$$\mathcal{D}_{\mathrm{total}} = \mathcal{D}_{\mathrm{mech}} + \mathcal{D}_{\mathrm{age}} \geq 0 \tag{50}$$

with each component individually non-negative, confirming thermodynamic consistency of the coupled mechanical–microstructural system.

The microstructural modulus H_ξ does not enter the mechanical equations; it affects only the stored energy accounting. Since the mechanical response depends solely on the threshold $\sigma_Y(\xi)$ through the yield function (16), ageing may be treated as a prescribed kinetic process without compromising the thermodynamic framework.

The first-order ageing kinetics (18) are written in general terms that do not presuppose a particular microstructural mechanism. For precipitation-hardening alloys, however, the ageing variable ξ admits a direct physical interpretation in terms of precipitate evolution. The Lifshitz–Slyozov–Wagner (LSW) coarsening theory gives the normalised precipitate state as

$$\bar{r}_n^3 - \bar{r}_{n,0}^3 = K_{\mathrm{LSW}}\cdot t \tag{51}$$

where K_{LSW} depends on the diffusion coefficient, interfacial energy, and temperature. The first-order kinetics adopted in (18) may be regarded as a linearised approximation valid during the initial hardening transient, before significant coarsening sets in. For extended ageing times approaching the over-ageing regime, higher-order kinetic descriptions would be needed; such extensions lie beyond the scope of the present work.

The complete system comprises the elasticity relation (10), back-stress definition (11), threshold-ageing coupling (17), ageing kinetics (18), flow rule (28), back-stress evolution (30), and strain partition (36)–(37). The material parameters governing the framework are listed in Table 1.

The framework reduces to classical Armstrong–Frederick kinematic hardening when $\tau_{\mathrm{rec}} \to \infty$ (no static recovery) and $\xi = 0$, $\sigma_Y = \sigma_{Y0}$ (no threshold evolution). Setting $H_\xi \to 0$ causes the ageing process to store no energy, so that

Table 1: Material parameters.

Symbol	Units	Physical Meaning
λ, μ	MPa	Lamé elastic constants
η	s	Viscous flow resistance
n	—	Stress exponent
σ_0	MPa	Reference stress
c	MPa	Kinematic hardening modulus
$\varkappa$	—	Dynamic recovery coefficient
τ_{rec}	s	Static recovery time
σ_{Y0}	MPa	Initial threshold
$\Delta\sigma_Y$	MPa	Threshold increment
τ_h	s	Hardening time constant
H_ξ	MPa	Microstructural hardening modulus

the microstructural dissipation $\mathcal{D}_{\text{age}}$ vanishes; the mechanical dissipation (45) is unaffected.

Although the individual equations in the preceding framework are drawn from established viscoplasticity theory, their coupling — specifically, the autonomous time evolution of σ_Y competing with the strain-driven evolution of $\boldsymbol{\chi}$ — gives rise to three distinct behavioural regimes, including flow arrest (defined in Section 1) in which inelastic flow initiates but subsequently ceases. These phenomena, which have not been analysed in the existing literature, are characterised in Section 3.

3. Competitive Hardening Dynamics

Within the constitutive framework of Section 2, two hardening mechanisms differ in their time dependence. The threshold stress $\sigma_Y(t)$ evolves autonomously with physical time, whereas the back stress $\boldsymbol{\chi}$ grows only during active inelastic flow, though static recovery may diminish it regardless of the flow state. The long-time deformation behaviour is accordingly governed by the competition between these two mechanisms.

3.1. Regime Classification

Under constant applied stress the back stress remains aligned with the deviatoric stress throughout monotonic loading, and the condition for inelastic flow, $\Sigma_{\text{eq}} > \sigma_Y$, reduces to a comparison between a scalar driving force and the total resistance to flow. The driving force is defined as

$$\mathcal{F}(t) = \|\boldsymbol{\sigma}'(t)\| \tag{52}$$

which is the deviatoric stress magnitude available to sustain flow. Under constant applied loading, $\mathcal{F}$ remains constant or changes only through stress redistribution. The total resistance is the sum of all mechanisms opposing flow, so that

$$\mathcal{R}(t) = \sigma_Y(t) + \chi_{\text{eq}}(t) \tag{53}$$

where $\chi_{\text{eq}} = \sqrt{\frac{3}{2}\boldsymbol{\chi} : \boldsymbol{\chi}}$ is the equivalent back stress. Inelastic flow then occurs when

$$\dot{p} > 0 \quad \Leftrightarrow \quad \mathcal{F} > \mathcal{R} \tag{54}$$

Since the two components of $\mathcal{R}$ evolve at different rates, we write their time derivatives, obtained from (20) and (30), as

$$\dot{\sigma}_Y = \frac{\Delta\sigma_Y}{\tau_h} e^{-t/\tau_h} \geq 0 \quad \text{always active} \tag{55}$$

$$\dot{\chi}_{\mathrm{eq}} = \sqrt{\frac{3}{2}}\frac{\boldsymbol{\chi} : \dot{\boldsymbol{\chi}}}{\chi_{\mathrm{eq}}} \quad \text{active only when } \dot{p} > 0 \tag{56}$$

The threshold stress therefore increases monotonically regardless of the mechanical loading state, approaching $\sigma_{Y\infty} = \sigma_{Y0} + \Delta\sigma_Y$ asymptotically. The back stress, in contrast, evolves only during active flow; if flow ceases, it either remains constant (when $\tau_{\mathrm{rec}} \to \infty$) or decays through static recovery.

The coupling between these two mechanisms produces a competition between time-driven hardening — $\sigma_Y(t)$ increasing continuously — and strain-driven hardening, in which $\boldsymbol{\chi}$ grows only during flow. Three long-time outcomes are then possible. If the resistance exceeds the driving force from the outset, no flow occurs (Regime I); if the resistance catches up at a finite time t^*, flow arrest takes place (Regime II); and if the driving force always exceeds the resistance, flow continues indefinitely (Regime III).

Two dimensionless parameters characterise the long-time behaviour. The load ratio

$$\Lambda = \frac{\sigma_{\mathrm{eff}}}{\sigma_{Y0}} \tag{57}$$

compares a characteristic applied stress σ_{eff} to the initial yield resistance, and the hardening capacity

$$\Gamma = \frac{\Delta\sigma_Y}{\sigma_{Y0}} \tag{58}$$

is the fractional increase in threshold stress from the initial to the saturated state; for precipitation-hardening aluminium alloys, typical values lie in the range 0.3–0.8.

To complete the description, two further dimensionless groups are introduced. The dimensionless time is

$$\Pi_t = \frac{t}{\tau_h} \tag{59}$$

and the back-stress saturation ratio is

$$\Pi_\chi = \frac{\chi_{\mathrm{sat}}}{\sigma_{Y0}} \tag{60}$$

in which $\chi_{\mathrm{sat}} = c/\varkappa$ is the upper bound of the saturation back stress, corresponding to the dynamic-recovery-dominated limit of (34).

In terms of these parameters, the flow condition at any instant becomes

$$\Lambda > 1 + \Gamma\left(1 - e^{-\Pi_t}\right) + \Pi_\chi\left(1 - e^{-\varkappa p}\right) \tag{61}$$

The two exponential terms on the right-hand side give the current fractional evolution of threshold stress and back stress respectively. For different values of Λ and Γ, the inequality (61) delineates three regimes. In Regime I ($\Lambda < 1$), the stress lies below the initial threshold and the response is purely elastic. In Regime II ($1 < \Lambda < 1 + \Gamma$), ageing-induced hardening arrests flow at a finite time. In Regime III ($\Lambda > 1 + \Gamma$), the stress exceeds the saturated threshold and flow continues indefinitely.

In the (Λ, Γ) parameter space the three regimes form a map that is of practical interest for process design. Regime II occupies a triangular region bounded by $\Lambda = 1$, $\Lambda = 1 + \Gamma$, and the positive Γ axis. For a given material (fixed Γ), the value of Λ determines whether arrest occurs; conversely, for a given loading condition, the hardening capacity Γ controls whether the flow can be arrested.

The regime boundaries stated above are necessary conditions that neglect the back-stress contribution. When kinematic hardening is included, the arrest regime expands, since the back stress provides additional resistance that reduces the effective driving force. The resulting acceleration of flow arrest is quantified in Section 3.3; the three-regime structure is displayed in Figure 5 as a phase map in the $(t/\tau_h, \Lambda)$ plane.

The gap between the two arrest boundaries in Figure 5 varies systematically with load ratio. It is widest at intermediate values ($\Lambda \approx 1 + \Gamma/2$), where the back stress has sufficient time to develop before arrest occurs. Near the upper boundary ($\Lambda \to 1 + \Gamma$), the back-stress contribution becomes negligible, since arrest occurs at increasingly late times when the threshold is already near saturation. Near the lower boundary ($\Lambda \to 1$), the brief flow duration limits

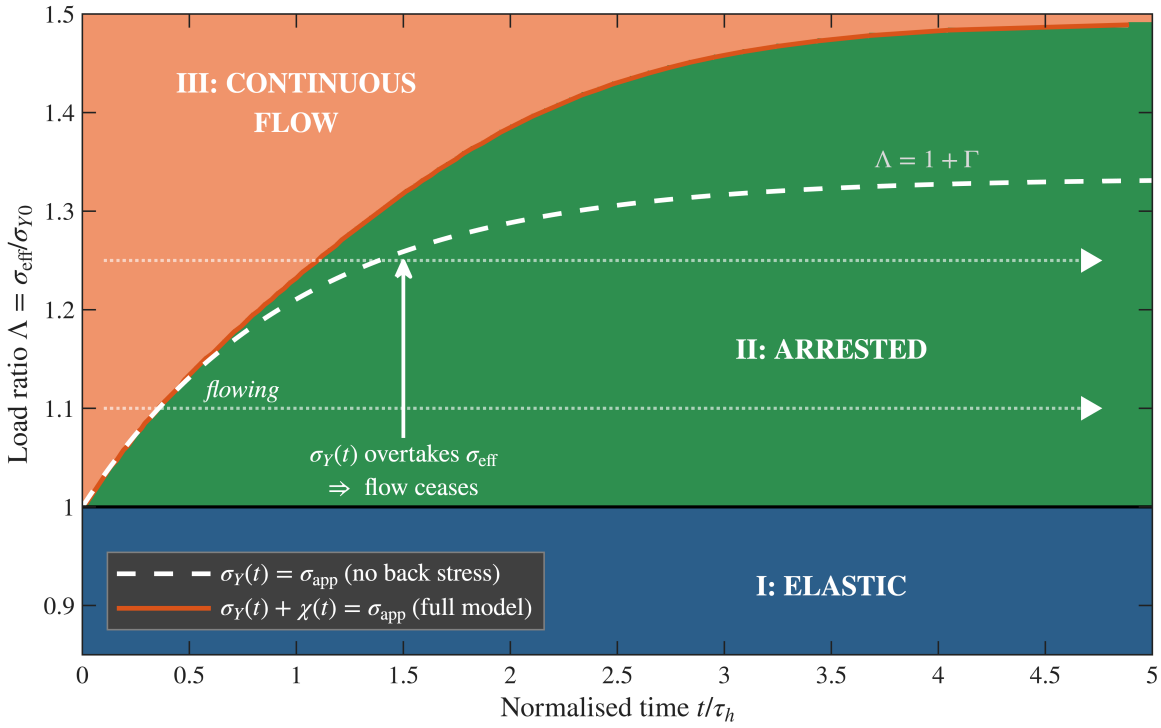

Figure 5: Three-regime state map in the $(t/\tau_h, \Lambda)$ plane showing elastic ($\Lambda < 1$, blue), arrested (green), and continuous-flow (coral) domains. At early times, material in Regime II flows transiently before arrest (coral wedge). Solid red curve: arrest boundary from the full model, $\sigma_Y(t) + \chi(t) = \sigma_{\text{app}}$. White dashed curve: arrest boundary neglecting back stress, $\sigma_Y(t) = \sigma_{\text{app}}$. The gap between the two boundaries corresponds to the acceleration effect discussed in Section 3.3; kinematic hardening reduces arrest time by providing immediate resistance that supplements the slower threshold evolution. Illustrative parameters with $\Pi_\chi = c/(\varkappa \sigma_{Y0}) = 0.33$.

back-stress accumulation. For the illustrative parameters shown, the back stress accelerates arrest by approximately $\Delta t^*/\tau_h \approx 0.3$ at $\Lambda = 1.25$.

Remark (degenerate case $\sigma_{Y0} = 0$). When the initial threshold vanishes, the dimensionless parameters Λ, Γ, and Π_χ defined in (57), (58), and (60) become undefined because each uses σ_{Y0} as the normalising stress. In this degenerate case the natural normalisation employs the asymptotic threshold $\sigma_{Y\infty} = \Delta\sigma_Y$, giving the reduced load ratio $\Lambda_\infty = \sigma_{\text{eff}}/\sigma_{Y\infty}$, the reduced back-stress ratio $\Pi_{\chi,\infty} = \chi_{\text{sat}}/\sigma_{Y\infty}$, and $\Gamma_\infty = 1$ by construction. The regime classification then simplifies to two cases — continuous flow ($\Lambda_\infty > 1$) and eventual arrest ($\Lambda_\infty < 1$) — with no purely elastic regime, since every nonzero stress exceeds the zero initial threshold. The arrest time (81) reduces to

$$\frac{t^*}{\tau_h} = -\ln(1 - \Lambda_\infty) \tag{62}$$

and all results of Sections 3.2–3.3 carry through with $\sigma_{Y\infty}$ replacing σ_{Y0} as the normalising stress. This case arises naturally in alloys where solution treatment produces a negligible initial dislocation barrier, so that the entire flow resistance develops through precipitation during ageing. Its occurrence in the calibration of Section 6 is discussed in Section 6.4.

3.2. Stability of Flow Arrest

A natural question is whether flow arrest, once achieved, is permanent. It is shown below that arrest constitutes a stable and irreversible transition; the argument proceeds by two routes — kinematic analysis and Lyapunov stability theory.

Flow arrest occurs when the overstress vanishes with a non-positive rate of change, so that

$$f(t^*) = 0 \quad \text{and} \quad \dot{f}(t^*) \le 0 \tag{63}$$

The first of these conditions marks the instant of arrest; the second precludes immediate resumption of flow.

To evaluate $\dot{f}$ at arrest, we differentiate the overstress function, giving

$$\dot{f} = \dot{\Sigma}_{\text{eq}} - \dot{\sigma}_Y \tag{64}$$

Under constant applied stress with an evolving back stress, the rate of effective stress follows from the chain rule as

$$\dot{\Sigma}_{\text{eq}} = \frac{\partial \Sigma_{\text{eq}}}{\partial \boldsymbol{\chi}} : \dot{\boldsymbol{\chi}} = -\frac{3}{2}\frac{\boldsymbol{\Sigma}}{\Sigma_{\text{eq}}} : \dot{\boldsymbol{\chi}} = -\mathbf{N} : \dot{\boldsymbol{\chi}} \tag{65}$$

The negative sign reflects the opposition between back stress and effective stress.

At the instant of arrest the viscoplastic multiplier $\dot{p} \to 0^+$ while remaining positive, the arrest being approached from active flow. Substituting into the back-stress evolution law (30) gives

$$\dot{\boldsymbol{\chi}}|_{\text{arrest}} = c\,\dot{p}\,\mathbf{N} - \varkappa\boldsymbol{\chi}\dot{p} - \frac{\boldsymbol{\chi}}{\tau_{\text{rec}}} \to -\frac{\boldsymbol{\chi}}{\tau_{\text{rec}}} \quad \text{as } \dot{p} \to 0^+ \tag{66}$$

The rate of effective stress at arrest is therefore

$$\dot{\Sigma}_{\text{eq}}|_{\text{arrest}} = -\mathbf{N} : \left(-\frac{\boldsymbol{\chi}}{\tau_{\text{rec}}}\right) = \frac{\mathbf{N} : \boldsymbol{\chi}}{\tau_{\text{rec}}} \tag{67}$$

Under monotonic loading from virgin conditions, both $\mathbf{N}$ and $\boldsymbol{\chi}$ point in the direction of the applied deviatoric stress — $\mathbf{N}$ because it is the flow direction, and $\boldsymbol{\chi}$ because it accumulates along the flow direction during prior deformation — so that $\mathbf{N} : \boldsymbol{\chi} > 0$ and hence $\dot{\Sigma}_{\text{eq}}|_{\text{arrest}} > 0$. It follows that the effective stress *increases* at the instant of arrest as a consequence of back-stress relaxation.

At arrest ($t = t^*$), the overstress rate is obtained from (64), (67), and (55) as

$$\dot{f}\Big|_{t^*} = \dot{\Sigma}_{\text{eq}}\Big|_{t^*} - \dot{\sigma}_Y(t^*) = \frac{\mathbf{N} : \boldsymbol{\chi}}{\tau_{\text{rec}}} - \frac{\Delta\sigma_Y}{\tau_h} e^{-t^*/\tau_h} \tag{68}$$

In the arrest regime (II) we have $\sigma_Y(t^*) < \sigma_{Y\infty}$, which requires

$$e^{-t^*/\tau_h} > 0 \tag{69}$$

The threshold stress accordingly continues to increase after arrest. Although Σ_{eq} also increases through back-stress relaxation (67), the threshold increases at a faster rate, provided the static recovery timescale is sufficiently large relative to the ageing timescale. After arrest, the back stress decays exponentially through static recovery, $\|\boldsymbol{\chi}(t)\| = \|\boldsymbol{\chi}(t^*)\| \exp[-(t-t^*)/\tau_{\text{rec}}]$, and the effective stress recovery rate is therefore bounded by $\|\boldsymbol{\chi}(t^*)\|/\tau_{\text{rec}}$. Arrest is strictly irreversible — in the sense that $\dot{f} \leq 0$ for all $t > t^*$ — when the threshold growth rate exceeds this recovery rate at $t = t^*$, which requires

$$\frac{\tau_{\text{rec}}}{\tau_h} > \frac{\|\boldsymbol{\chi}(t^*)\|}{\Delta\sigma_Y\, e^{-t^*/\tau_h}} \tag{70}$$

For all physically relevant parameter combinations in which $\tau_{\text{rec}} \gg \tau_h$ — as is the case for the material systems considered here — the condition (70) is satisfied. The threshold growth rate at arrest is given by

$$\dot{\sigma}_Y(t^*) = \frac{\sigma_{Y\infty} - \sigma_Y(t^*)}{\tau_h} > 0 \tag{71}$$

In the absence of static recovery, both the stress and the back-stress distributions become time-independent after arrest. Even when τ_{rec} is finite, the total stress $\boldsymbol{\sigma}$ remains frozen because the elastic strain compensates for back-stress relaxation through (10). The final stress state consequently depends on the arrest time t^* rather than on asymptotic values, and process design must account for the transient evolution, not merely for the steady-state parameters.

An alternative route to establishing irreversibility is provided by Lyapunov's direct method, which offers an energy-based perspective and establishes asymptotic stability in addition to permanence. Consider the total stored energy functional

$$V(t) = \int_\Omega \left[\frac{1}{2}\boldsymbol{\varepsilon}^{\text{e}} : \mathbb{C} : \boldsymbol{\varepsilon}^{\text{e}} + \frac{1}{2c}\boldsymbol{\chi} : \boldsymbol{\chi} + \frac{H_\xi}{2}(\xi - 1)^2 \right] dV \tag{72}$$

where Ω denotes the material domain and dV the volume element. The three terms are, in order, the elastic strain energy, the kinematic hardening energy stored in dislocation structures, and the microstructural ageing energy. By construction $V \geq 0$, with equality holding only when $\varepsilon^{\text{e}} = 0, \chi = 0$, and $\xi = 1$.

Differentiating with respect to time gives

$$\dot{V} = \int_\Omega \left[\boldsymbol{\sigma} : \dot{\boldsymbol{\varepsilon}}^{\text{e}} + \frac{1}{c}\boldsymbol{\chi} : \dot{\boldsymbol{\chi}} + H_\xi(\xi - 1)\dot{\xi} \right] dV \tag{73}$$

On substituting the strain decomposition $\dot{\boldsymbol{\varepsilon}}^{\text{e}} = \dot{\boldsymbol{\varepsilon}} - \dot{\boldsymbol{\varepsilon}}^{\text{in}}$, the stress power may be written as

$$\boldsymbol{\sigma} : \dot{\boldsymbol{\varepsilon}}^{\text{e}} = \boldsymbol{\sigma} : \dot{\boldsymbol{\varepsilon}} - \boldsymbol{\sigma} : \dot{\boldsymbol{\varepsilon}}^{\text{in}} \tag{74}$$

Under constant applied loading the quantity $\boldsymbol{\sigma} : \dot{\boldsymbol{\varepsilon}}$ equals the external power input P_{ext}, and substitution of the dissipation components yields

$$\dot{V} = P_{\text{ext}} - \mathcal{D}_{\text{total}} \tag{75}$$

in which $\mathcal{D}_{\text{total}}$ is the total dissipation defined in (47).

At arrest under constant applied stress, the total strain rate vanishes ($\dot{\boldsymbol{\varepsilon}} = \dot{\boldsymbol{\varepsilon}}^{\text{e}} + \dot{\boldsymbol{\varepsilon}}^{\text{in}} = \mathbf{0}$, both contributions being frozen), so that the external power $P_{\text{ext}} = \boldsymbol{\sigma} : \dot{\boldsymbol{\varepsilon}} = 0$. The energy rate therefore reduces to

$$\dot{V}|_{\text{arrest}} = -\mathcal{D}_{\text{stat}} - \mathcal{D}_{\text{age}} = -\frac{\|\boldsymbol{\chi}\|^2}{c\,\tau_{\text{rec}}} - \frac{H_\xi}{\tau_h}(1 - \xi)^2 \leq 0 \tag{76}$$

with equality only when $\chi = 0$ and $\xi = 1$. The functional V is positive definite in the neighbourhood of the equilibrium and decreases along trajectories ($\dot{V} \leq 0$), reaching $\dot{V} = 0$ only at the equilibrium point itself. By

Lyapunov's direct method, the arrested state is asymptotically stable. It may be noted that V does not vanish at the post-arrest equilibrium: the elastic strain energy $(1/2)\boldsymbol{\varepsilon}^{\mathrm{e}} : \mathbb{C} : \boldsymbol{\varepsilon}^{\mathrm{e}}$ remains positive (and constant) after arrest, the stress field being frozen. The stability conclusion follows because the only dynamically evolving contributions — the back-stress energy and the ageing energy — decrease monotonically through $\mathcal{D}_{\mathrm{stat}}$ and $\mathcal{D}_{\mathrm{age}}$, reaching zero only at the equilibrium $\boldsymbol{\chi} = \mathbf{0}$, $\xi = 1$.

Arrested states act as energy sinks; stored energy associated with back stress and incomplete ageing is dissipated through static recovery and continued ageing. The system evolves toward the minimum-energy configuration in which $\boldsymbol{\chi} \to 0$ and $\xi \to 1$. After arrest, the stored energy decreases monotonically, so that

$$V(t_2) < V(t_1) \quad \text{for all } t_2 > t_1 > t^* \tag{77}$$

unless $\boldsymbol{\chi}(t_1) = \mathbf{0}$ and $\xi(t_1) = 1$.

3.3. Kinematic Hardening Acceleration Effect

Kinematic hardening not only contributes to flow arrest but accelerates its occurrence. To establish a baseline, consider first the case without kinematic hardening ($\boldsymbol{\chi} \equiv 0$). The arrest condition then takes the form

$$\sigma_{\mathrm{eff}} = \sigma_Y\left(t_0^*\right) \tag{78}$$

where t_0^* denotes the arrest time in the absence of back stress. Substituting the threshold evolution (20) furnishes

$$\sigma_{\mathrm{eff}} = \sigma_{Y0} + \Delta\sigma_Y\left(1 - e^{-t_0^*/\tau_h}\right) \tag{79}$$

Solving for the arrest time, we obtain

$$t_0^* = -\tau_h \ln\left(1 - \frac{\sigma_{\mathrm{eff}} - \sigma_{Y0}}{\Delta\sigma_Y}\right) = -\tau_h \ln\left(\frac{\sigma_{Y\infty} - \sigma_{\mathrm{eff}}}{\Delta\sigma_Y}\right) \tag{80}$$

In dimensionless form this becomes

$$\frac{t_0^*}{\tau_h} = -\ln\left(1 - \frac{\Lambda - 1}{\Gamma}\right) \tag{81}$$

For this solution to exist ($t_0^* > 0$ and finite), it is necessary that

$$0 < \frac{\Lambda - 1}{\Gamma} < 1 \quad \Leftrightarrow \quad 1 < \Lambda < 1 + \Gamma \tag{82}$$

which recovers the Regime II condition established in Section 3.1.

In view of (63), when kinematic hardening is present the arrest condition becomes

$$\sigma_{\mathrm{eff}} - \chi_{\mathrm{eq}}(t^*) = \sigma_Y(t^*) \tag{83}$$

Because $\chi_{\mathrm{eq}}(t^*) > 0$, the threshold stress required at arrest is smaller than in the baseline case, namely

$$\sigma_Y(t^*) = \sigma_{\mathrm{eff}} - \chi_{\mathrm{eq}}(t^*) < \sigma_{\mathrm{eff}} = \sigma_Y\left(t_0^*\right) \tag{84}$$

From the monotonicity of the threshold evolution (20), it follows that

$$t^* < t_0^* \tag{85}$$

Kinematic hardening hence accelerates flow arrest strictly ($t^* < t_0^*$).

To quantify the acceleration, we write (79) with the back stress included, giving

$$\sigma_{\mathrm{eff}} - \chi_{\mathrm{eq}}(t^*) = \sigma_{Y0} + \Delta\sigma_Y\left(1 - e^{-t^*/\tau_h}\right) \tag{86}$$

Solving for t^* yields

$$t^* = -\tau_h \ln\left(\frac{\sigma_{Y\infty} - \sigma_{\text{eff}} + \chi_{\text{eq}}(t^*)}{\Delta\sigma_Y}\right) \tag{87}$$

The ratio of arrest times is then

$$\frac{t^*}{t_0^*} = \frac{\ln\left[\Delta\sigma_Y / \left(\sigma_{Y\infty} - \sigma_{\text{eff}} + \chi_{\text{eq}}\right)\right]}{\ln\left[\Delta\sigma_Y / \left(\sigma_{Y\infty} - \sigma_{\text{eff}}\right)\right]} < 1 \tag{88}$$

The strict inequality holds because $\chi_{\text{eq}} > 0$ makes the argument of the logarithm in the numerator smaller than that in the denominator.

In the limit of small back stress ($\chi_{\text{eq}} \ll \sigma_{Y\infty} - \sigma_{\text{eff}}$), a first-order expansion of the numerator furnishes

$$\frac{t^*}{t_0^*} \approx 1 - \frac{\chi_{\text{eq}}}{\sigma_{Y\infty} - \sigma_{\text{eff}}} \cdot \frac{1}{\ln\left[\Delta\sigma_Y / \left(\sigma_{Y\infty} - \sigma_{\text{eff}}\right)\right]} \tag{89}$$

so that the relative acceleration is proportional to χ_{eq} and inversely proportional to the overstress margin $\sigma_{Y\infty} - \sigma_{\text{eff}}$.

When the back stress reaches its saturation value ($\chi_{\text{eq}} \to \chi_{\text{sat}} = c/\varkappa$), the acceleration is greatest and the ratio attains its minimum value

$$\frac{t^*_{\text{min}}}{t_0^*} = \frac{\ln\left[\Delta\sigma_Y / \left(\sigma_{Y\infty} - \sigma_{\text{eff}} + c/\varkappa\right)\right]}{\ln\left[\Delta\sigma_Y / \left(\sigma_{Y\infty} - \sigma_{\text{eff}}\right)\right]} \tag{90}$$

The magnitude of the acceleration depends on the dimensionless ratio $c/(\varkappa\Delta\sigma_Y)$ and on the position within Regime II; the reduction is greatest at intermediate load ratios where the back stress has sufficient time to develop before arrest, and vanishes near the regime boundaries. The actual acceleration for a given trajectory is smaller than the upper bound (90), because $\chi_{\text{eq}}(t^*) < c/\varkappa$ when arrest occurs before back-stress saturation; the applicability of this acceleration to the material system studied here is discussed in Section 6. Physically, the back stress provides immediate resistance that complements the slower threshold evolution. Whereas σ_Y requires a time of order τ_h to approach saturation, the back stress develops rapidly during the initial flow transient; this early resistance permits arrest at a lower threshold value and hence at an earlier time. The yield surface translation and the resulting tension–compression asymmetry are illustrated in Figure 6 for three representative load ratios.

Figure 6 shows the mechanical consequences of kinematic hardening in stress space. During loading (panel a), the yield surface translates in the direction of the applied stress by an amount equal to the current back stress; the translation increases with Λ because higher stress levels produce faster inelastic strain accumulation and consequently faster back-stress growth. Upon unloading to zero stress (panel b), the translated surfaces show that the reverse yield stress — the compressive stress required to reinitiate flow — is reduced by twice the back stress, producing the Bauschinger effect. In panel (c), the back-stress trajectories follow the Armstrong–Frederick saturation dynamics; the two continuous-flow cases ($\Lambda = 1.50, 1.80$) approach the common plateau $\chi_{\text{sat}} = c/\varkappa$ at different rates, while the arrested case ($\Lambda = 1.20$) freezes well below saturation when flow ceases. The tension–compression asymmetry quantified in panel (d) grows with Λ because the back stress at the evaluation time increases with the accumulated inelastic strain; this asymmetry is a prediction of the constitutive framework and would be absent in a purely isotropic hardening model.

4. Physics-Informed Neural Network Formulation

The constitutive framework of Sections 2–3 poses three difficulties for conventional numerical integration. The yield transition at the Macaulay bracket is non-smooth; the time scales span several orders of magnitude; and the boundaries between active and arrested regions shift as the threshold stress increases. The Macaulay bracket appearing in the flow rule (28) is defined by

$$\langle x \rangle = \max(0, x) = \begin{cases} x & x > 0 \\ 0 & x \le 0 \end{cases} \tag{91}$$

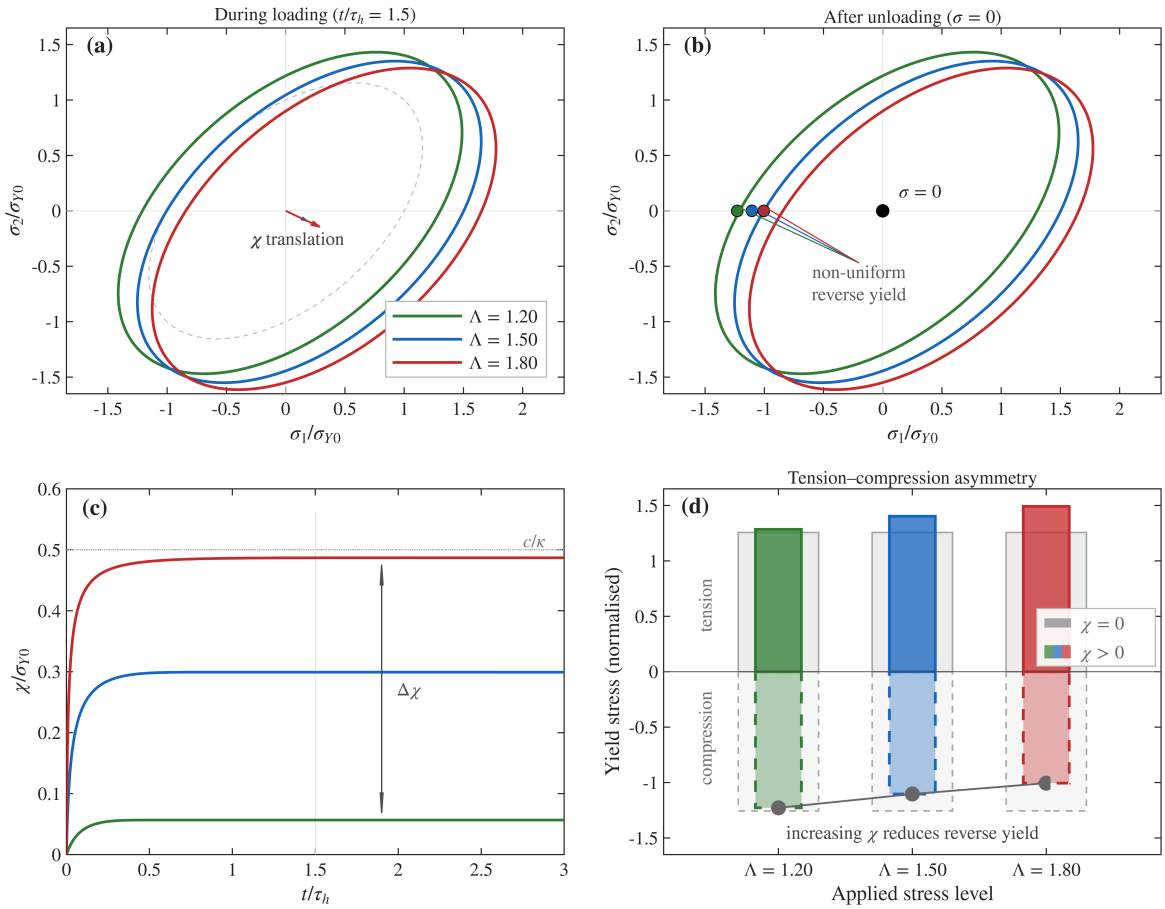

Figure 6: Yield surface evolution under kinematic hardening at three load ratios ($\Lambda = 1.20, 1.50, 1.80$): (a) translated von Mises surfaces during loading at $t/\tau_h = 1.5$, showing χ-induced translation; (b) after unloading to $\sigma = 0$, showing non-uniform reverse yield points; (c) back-stress time histories $\chi(t)/\sigma_{Y0}$, showing approach to saturation at $c/\varkappa$ for continuous-flow cases and frozen sub-saturation values for the arrested case; (d) tension–compression asymmetry bar chart showing that increasing χ reduces reverse yield stress (Bauschinger effect).

and its derivative is discontinuous at $x = 0$. In classical finite element implementations the discontinuity is handled through return-mapping algorithms, but neural network-based methods require a smooth approximation because gradients must propagate through the yield transition during backpropagation. The softplus function furnishes such an approximation,

$$\langle x \rangle_k \approx \frac{1}{k} \ln\left(1 + e^{kx}\right) \tag{92}$$

where $k > 0$ controls the sharpness of the transition. Differentiating (92) gives

$$\frac{d\langle x \rangle_k}{dx} = \frac{1}{1 + e^{-kx}} = \sigma(kx) \tag{93}$$

in which $\sigma(\cdot)$ denotes the sigmoid function; derivatives are accordingly continuous for all finite k. The softplus function was introduced by Dugas et al. [88] to impose monotonicity and convexity constraints in neural networks, and is adopted here as a smooth surrogate for the Macaulay bracket. During training the sharpness parameter k is progressively increased through a curriculum learning strategy analogous to continuation methods in computational plasticity [89], in which a regularised problem is solved first and the original non-smooth problem is recovered gradually.

A mesh-free alternative is provided by PINNs, in which the governing equations enter as soft constraints while selected physical requirements — initial conditions and incompressibility — are satisfied exactly through the network architecture. The general tensor formulation is set out first; the implementation then specialises to a parametric material point case.

4.1. Network Architecture

For the general tensor formulation the neural network approximates the solution fields as continuous functions of the coordinate–time tuple $(\mathbf{x}, t)$,

$$\mathcal{N}_\theta : (\mathbf{x}, t) \mapsto \left\{u_i,\, \varepsilon^{\text{in}}_{ij},\, \chi_{ij}\right\} \tag{94}$$

where θ denotes the trainable network parameters, u_i are displacement components, $\varepsilon^{\text{in}}_{ij}$ is the accumulated inelastic strain tensor, and χ_{ij} is the back-stress tensor. Because the constitutive residuals require the inelastic strain rate and the back-stress rate, both are obtained by automatic differentiation of the network outputs, $\dot{\varepsilon}^{\text{in}}_{ij} = \partial \varepsilon^{\text{in}}_{ij}/\partial t$ and $\dot{\chi}_{ij} = \partial \chi_{ij}/\partial t$; numerical time integration is accordingly unnecessary, and both evolution equations receive identical treatment.

When the formulation is specialised to a single material point under prescribed uniaxial stress, the spatial coordinates are absent and the network input reduces to the pair $(\bar{\sigma}, \bar{t})$. Here $\bar{\sigma} = \sigma/\sigma_{Y0}$ is the normalised applied stress, coinciding with the load ratio Λ defined in Section 3.1 for uniaxial loading, and $\bar{t} = t/\tau_h$ is the normalised time. Since the stress level enters as a network input alongside time, the PINN is formulated as a single parametric map,

$$\mathcal{N}_\theta : (\bar{\sigma}, \bar{t}) \mapsto \left\{\varepsilon^{\text{in}},\, \chi\right\} \tag{95}$$

over the full stress–time domain $\bar{\sigma} \in [0.85, 1.50]$, which spans the elastic, arrest, and continuous flow regimes identified in Section 3.1. The parametric formulation therefore encodes the complete competitive hardening response in a single network rather than requiring a separate solution for each stress level, and generalises to unseen stress values within the training range without retraining.

Because the two inputs operate on different scales, both must be mapped to a common range before training. The stress input is centred and scaled to $[-1, 1]$, and the time input is treated similarly, giving

$$\tilde{\sigma} = \frac{\bar{\sigma} - \bar{\sigma}_{\text{mid}}}{\bar{\sigma}_{\text{half}}}, \qquad \tilde{t} = \frac{2\bar{t}}{T_{\text{end}}/\tau_h} - 1 \tag{96}$$

where $\bar{\sigma}_{\text{mid}} = (\bar{\sigma}_{\max} + \bar{\sigma}_{\min})/2 = 1.175$ and $\bar{\sigma}_{\text{half}} = (\bar{\sigma}_{\max} - \bar{\sigma}_{\min})/2 = 0.325$, and $T_{\text{end}} = 5\tau_h$, so that the time input spans $[-1, 1]$ over the full simulation horizon. Both mapped inputs then fall within the natural operating range of the hyperbolic tangent activation, avoiding the slow convergence associated with unnormalised inputs.

Under Xavier initialisation with bounded tanh activation the raw network outputs are $O(0.1)$, whereas the physical fields span many orders of magnitude — $\varepsilon^{\text{in}} \sim O\left(10^{-8}\right)$ and $\chi \sim O\left(10^{4}\right)$ Pa. Without output scaling, the optimiser must suppress the raw outputs by seven or more decades to reach the correct solution, and training becomes trapped in trivial local minima. Physical characteristic scales are therefore introduced, so that

$$\hat{\varepsilon}^{\text{in}} = \mathcal{N}_\theta^{\varepsilon} \cdot s_\varepsilon, \qquad \hat{\chi} = \mathcal{N}_\theta^{\chi} \cdot s_\chi, \qquad s_\varepsilon = \frac{\tau_h}{\eta}\left(\frac{\bar{\sigma}_{\text{mid}}\,\sigma_{Y0} - \sigma_{Y0}}{\sigma_0}\right)^n, \qquad s_\chi = c\, s_\varepsilon \tag{97}$$

Here s_ε is the characteristic inelastic strain accumulated at a representative overstress over one ageing time, and $s_\chi = c\, s_\varepsilon$ reflects the initial-growth proportionality $\chi \approx c\,\varepsilon^{\text{in}}$ that holds before dynamic and static recovery become significant. It may be noted that the input and output normalisations defined in (96)–(97) require $\sigma_{Y0} > 0$; when the initial threshold vanishes, the alternative normalisation using $\sigma_{Y\infty}$ described in the Remark of Section 3.1 applies.

A shared-trunk, dual-head architecture is adopted for the network. A single trunk of six fully connected layers (512 neurons each) processes the normalised inputs $\left(\tilde{\sigma}, \tilde{t}\right)$ and produces a shared feature representation; two independent linear heads then project this representation onto the scalar outputs ε^{in} and χ respectively, with physical output scaling (97) and hard initial condition enforcement via output subtraction (104). Since automatic differentiation of the physics residuals requires smooth gradients, the hyperbolic tangent is used as the activation function throughout the trunk, yielding derivatives that are continuous to all orders. Each head is initialised with a reduced gain (0.1 instead of 1.0), permitting the two outputs to be calibrated independently without one field dominating the trunk gradients in early training. The total parameter count is approximately 1.57×10^6; the complete architecture is depicted in Figure 7.

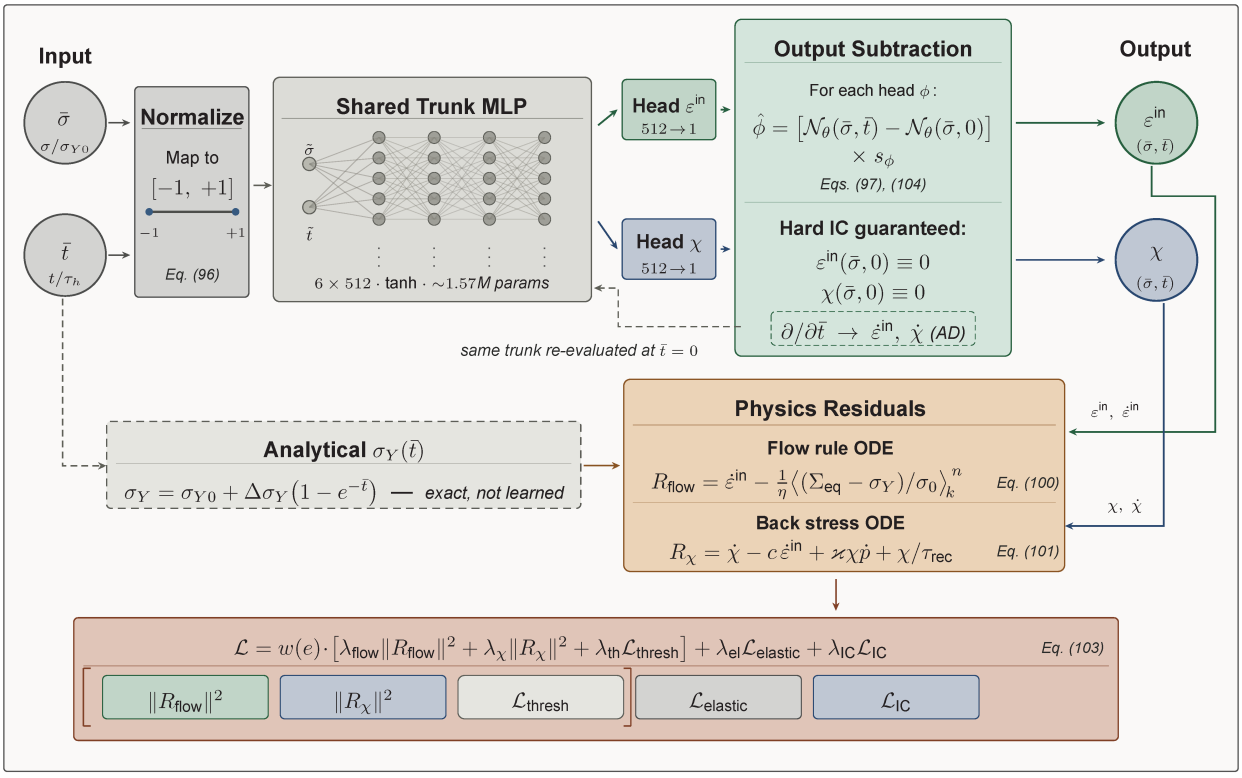

Figure 7: Architecture of the parametric physics-informed neural network: normalised inputs $(\bar{\sigma}, \bar{t})$ mapped to $[-1, 1]$, shared trunk MLP (6×512, tanh), dual output heads for ε^{in} and χ, output subtraction enforcing hard initial conditions, analytical threshold stress $\sigma_Y(\bar{t})$ as known input to physics residuals, and composite loss function with five penalty terms.

Three features of the architecture in Figure 7 warrant comment. Because the trunk is shared between both output fields, the network encodes the coupling between ε^{in} and χ through common internal representations; the separate

heads then allow independent scaling and initialisation for each field. The output subtraction loop — in which the trunk is evaluated at both $\bar{t}$ and $\bar{t} = 0$ for the same stress input — imposes the initial conditions $\varepsilon^{\text{in}}(0) = 0$ and $\chi(0) = 0$ exactly, regardless of the network parameters. The threshold stress $\sigma_Y(\bar{t})$ bypasses the network entirely and enters the physics residuals as an analytical function computed from (20); the time-autonomous ageing kinetics are consequently represented exactly rather than approximated, and no approximation error is introduced into the thermodynamic structure established in Section 2.

Inelastic deformation in metals is volume-preserving, so that $\operatorname{tr}\left(\boldsymbol{\varepsilon}^{\text{in}}\right) = 0$. In spatially extended problems the trace-free condition is satisfied exactly by restricting the network output to the independent deviatoric components; the remaining component is then recovered from the constraint. Since $\operatorname{tr}(\boldsymbol{\chi}) = 0$ follows from $\boldsymbol{\chi} = c\,\boldsymbol{\varepsilon}^{\text{an}}$ and anelastic incompressibility, the same deviatoric parameterisation applies to the back-stress tensor. In the scalar uniaxial case both constraints are trivially satisfied.

4.2. Physics Residuals and Loss Function

The governing equations of Section 2 are incorporated into the loss function as physics residuals evaluated at collocation points distributed over the $(\bar{\sigma}, \bar{t})$ domain. In the material point formulation spatial gradients are absent and only the constitutive residuals are active; the equilibrium and elastic constitutive residuals arise in the general spatial formulation and are stated here for completeness. In the absence of body forces, momentum balance gives

$$\mathcal{R}_{\text{eq}}^{(j)} = \frac{\partial \sigma_{ij}}{\partial x_i} = 0 \tag{98}$$

where stress is computed from the elastic constitutive relation (10). The stress–strain relation yields the elastic residual

$$\mathcal{R}_{\text{el}}^{(ij)} = \sigma_{ij} - C_{ijkl}\left(\varepsilon_{kl} - \varepsilon_{kl}^{\text{in}}\right) \tag{99}$$

Both residuals vanish identically in the material point case. In view of the smooth Macaulay bracket approximation (92), the viscoplastic flow rule (28) takes the residual form

$$\mathcal{R}_{\text{flow}}^{(ij)} = \dot{\varepsilon}_{ij}^{\text{in}} - \frac{1}{\eta}\left\langle \frac{\Sigma_{\text{eq}} - \sigma_Y(t)}{\sigma_0} \right\rangle_k^n \frac{3}{2}\frac{\Sigma_{ij}}{\Sigma_{\text{eq}} + \epsilon} \tag{100}$$

where $\Sigma_{ij} = \sigma'_{ij} - \chi_{ij}$ is the effective stress deviator (14), Σ_{eq} its equivalent value (15), and $\epsilon > 0$ is a small regularisation constant (typically 10^{-8}) that prevents division by zero when $\Sigma_{\text{eq}} \to 0$. From the modified Armstrong–Frederick equation (30) with static recovery, the back-stress residual becomes

$$\mathcal{R}_{\chi}^{(ij)} = \dot{\chi}_{ij} - c\dot{\varepsilon}_{ij}^{\text{in}} + \varkappa \chi_{ij}\dot{p} + \frac{\chi_{ij}}{\tau_{\text{rec}}} \tag{101}$$

where $\dot{p} = \sqrt{(2/3)\dot{\varepsilon}_{ij}^{\text{in}}\dot{\varepsilon}_{ij}^{\text{in}}}$ is the equivalent inelastic strain rate (29). The rates $\dot{\varepsilon}_{ij}^{\text{in}}$ and $\dot{\chi}_{ij}$ appearing in both (100) and (101) are obtained by automatic differentiation of the network outputs with respect to time; numerical time integration is therefore avoided entirely.

The total loss combines five weighted contributions that address distinct aspects of the constitutive response. With the mean squared residual over N_c collocation points denoted by

$$\|\mathcal{R}\|^2 = \frac{1}{N_c}\sum_{i=1}^{N_c} \left|\mathcal{R}\left(\bar{\sigma}_i, \bar{t}_i\right)\right|^2 \tag{102}$$

the total loss may be written

$$\mathcal{L} = w(e)\left[\lambda_{\text{flow}}\|\mathcal{R}_{\text{flow}}\|^2 + \lambda_{\chi}\|\mathcal{R}_{\chi}\|^2 + \lambda_{\text{th}}\mathcal{L}_{\text{thresh}}\right] + \lambda_{\text{el}}\mathcal{L}_{\text{elastic}} + \lambda_{\text{IC}}\mathcal{L}_{\text{IC}} \tag{103}$$

The physics residuals $\|\mathcal{R}_{\text{flow}}\|^2$ and $\|\mathcal{R}_{\chi}\|^2$ enforce the flow rule (100) and back-stress evolution (101) at $N_c = 8{,}000$ collocation points sampled uniformly from the full $(\bar{\sigma}, \bar{t})$ domain. Because the smooth Macaulay bracket residual is

most sensitive to the sharpness parameter k near the yield boundary, a near-threshold penalty $\mathcal{L}_{\text{thresh}}$ evaluates the flow and back-stress residuals at a further $N_{\text{th}} = 1{,}800$ points concentrated in the range $\bar{\sigma} \in [1.0, 1.15]$, compensating for the small fraction of the domain that lies near threshold. Within the elastic region ($\bar{\sigma} < 1$) the penalty $\mathcal{L}_{\text{elastic}}$ imposes $\hat{\varepsilon}^{\text{in}} \approx 0$ and $\hat{\chi} \approx 0$ at $N_{\text{el}} = 1{,}000$ points; the physics residuals are inactive there and the smooth bracket approximation does not identically vanish; without this term the network may assign spurious non-zero strains to sub-threshold loading states. The hard output subtraction constraint is supplemented by an auxiliary IC loss $\mathcal{L}_{\text{IC}}$, a redundant soft penalty that drives $\hat{\varepsilon}^{\text{in}}(\bar{\sigma}, 0)$ and $\hat{\chi}(\bar{\sigma}, 0)$ to zero at 200 stress levels.

The initial conditions $\varepsilon^{\text{in}}(0) = 0$, $\chi(0) = 0$ are imposed exactly through the network architecture by output subtraction. For each head output $\hat{\phi}$, the subtracted form is

$$\hat{\phi}(\bar{\sigma}, \bar{t}) = [\mathcal{N}_\theta(\bar{\sigma}, \bar{t}) - \mathcal{N}_\theta(\bar{\sigma}, 0)] \cdot s_\phi \tag{104}$$

and it follows that $\hat{\phi}(\bar{\sigma}, 0) = 0$ for all stress levels regardless of the network parameters θ. In practice the trunk is called at $\bar{t} = 0$ for the same stress batch, and the difference is taken before applying the physical scale; the constraint is thus evaluated parametrically across the entire stress range. Enforcement by soft penalty alone was found to produce persistent initial condition violations that corrupted the solution throughout the domain, and the hard subtraction proved indispensable for stable training.

The regime classification of Section 3.1 informs the collocation strategy directly. Because the elastic ($\Lambda < 1$), arrest ($1 < \Lambda < 1 + \Gamma$), and continuous flow ($\Lambda > 1 + \Gamma$) states exhibit qualitatively different behaviour, the three-zone sampling — general, threshold, and elastic — is designed so that the network encounters all three regimes during every training iteration.

4.3. Training Strategy

The smooth Macaulay bracket (92) introduces a systematic approximation error that depends on k. Near the arrest boundary the normalised overstress $x \to 0^+$, and the sigmoid factor $\sigma(kx)$ deviates appreciably from unity unless k is large. A curriculum strategy is accordingly adopted in which k is progressively increased from $k_0 = 5$ to $k_f = 100$ over the course of training, giving

$$k(e) = \begin{cases} k_0 + (20 - k_0)\,\frac{e}{0.2\,E} & e < 0.2\,E \\ 20 + 30\,\frac{e - 0.2E}{0.3\,E} & 0.2\,E \le e < 0.5\,E \\ 50 + \left(k_f - 50\right)\,\frac{e - 0.5E}{0.5\,E} & e \ge 0.5\,E \end{cases} \tag{105}$$

where e is the current epoch and E is the total epoch count. The schedule comprises three phases: the first establishes approximate flow behaviour at low sharpness, the second refines the yield transition at intermediate values, and the third sharpens to the target. Figure 8 shows the smooth approximation and its derivative for several values of the sharpness parameter.

As k increases in Figure 8(a), the smooth approximation converges uniformly to the exact Macaulay bracket, with the transition region narrowing proportionally to $1/k$. The corresponding derivative in panel (b) approaches the Heaviside step function; the sigmoid activation $\sigma(kx)$ hence provides a continuous gradient even at the yield point — a property on which backpropagation relies. At $k = 35$ the approximation error is confined to a narrow band $|x| < 0.1$, substantially smaller than the overstress values encountered in the flowing regime. The curriculum strategy exploits this uniform convergence by beginning training at low k, where the smooth gradients permit rapid initial learning, and progressing to high k, where the sharp transition is needed to resolve the arrest boundary accurately.

A complementary curriculum ramps the combined physics weight $w(e)$ in Eq. (103) from 1 to 10 over the first 30% of training, so that

$$w(e) = 1 + 9 \cdot \min\left(1,\, \frac{e}{0.3\,E}\right) \tag{106}$$

The ramp permits the elastic zone and IC penalties to regularise the solution before the physics residuals are fully activated. Without it, the large initial physics residuals were observed to overwhelm the IC and elastic penalties, leading to solutions that satisfied the ODE in the flowing regime but violated the zero-strain condition at threshold.

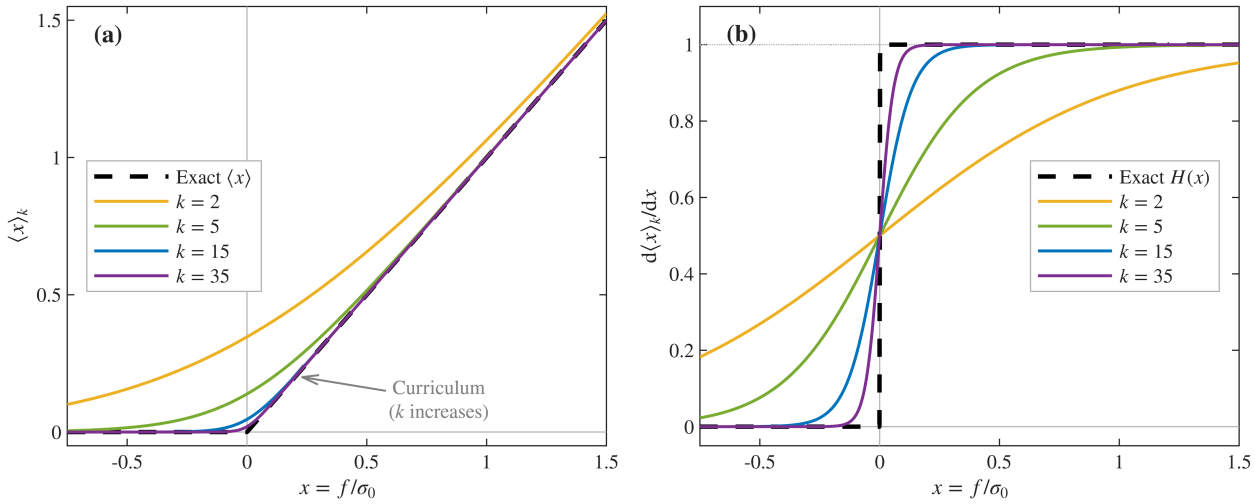

Figure 8: Smooth Macaulay bracket approximation $\langle x \rangle_k$ (a) and its derivative $d\langle x \rangle_k/dx$ (b) for increasing sharpness parameter $k = 2, 5, 15, 35$. The curriculum learning schedule increases k from $k_0 = 5$ to $k_f = 100$ during training, progressively sharpening the elastic–inelastic transition.

Hyperparameter optimisation was carried out within the Optuna framework using 40 trials of 30,000 epochs each. The search space comprised network width $\in \{256, 512, 1024\}$, depth $\in \{4, 6, 8\}$, learning rate, loss weights, and the effective static recovery timescale $\tau_{\mathrm{rec}}^{\mathrm{eff}} \in \left[5 \times 10^5,\ 5 \times 10^6\right]$ s. As a starting point, the study was warm-started with the best configuration from the simpler single-output baseline ($\varepsilon^{\mathrm{in}}$ only), which achieved $L^2 = 4.21\%$. The search did not improve upon this warm-start configuration (512×6 trunk, $\ell_r = 8 \times 10^{-4}$), suggesting that architecture requirements are governed by the underlying constitutive complexity rather than the number of outputs. The best configuration was then retrained for 300,000 epochs on the SGDR schedule (Cosine Annealing Warm Restarts with $T_0 = 20{,}000$, $T_{\mathrm{mult}} = 2$, $\eta_{\min} = 0.02\,\ell_r$), giving restart boundaries at epochs 20k, 60k, 140k, and 300k. Table 2 summarises the complete training configuration.

Table 2: Training configuration for the parametric coupled PINN.

Parameter	Value
Optimiser	Adam ($\beta_1 = 0.9, \beta_2 = 0.999$)
Initial learning rate ℓ_r	8×10^{-4}
Learning rate schedule	SGDR: $T_0 = 20{,}000$, $T_{\mathrm{mult}} = 2$, $\eta_{\min} = 0.02\,\ell_r$
Total epochs	300,000
General collocation N_c	8,000 (uniform in $(\bar{\sigma}, \bar{t})$ domain)
Threshold collocation N_{th}	1,800 (biased: $\bar{\sigma} \in [1.0, 1.15]$)
Elastic collocation N_{el}	1,000 (elastic zone: $\bar{\sigma} < 1$)
IC enforcement	Hard (output subtraction, Eq. (104)) + soft $\mathcal{L}_{\mathrm{IC}}$
Sharpness curriculum	$k_0 = 5 \to k_f = 100$ via Eq. (105)
Physics weight ramp	$w : 1 \to 10$ over first 30% of epochs (Eq. (106))
Gradient clipping	ℓ^2-norm ≤ 1.0
Network initialisation	Xavier uniform (trunk); reduced gain 0.1 (heads)
Arithmetic precision	float32

The accuracy of the trained network is measured by the L^2 relative error between PINN predictions and high-accuracy reference solutions obtained from a Radau IIA integrator ($r_{\mathrm{tol}} = 10^{-10}$, $a_{\mathrm{tol}} = 10^{-13}$),

$$\epsilon_{L^2}^2 = \frac{\|\phi_{\mathrm{PINN}} - \phi_{\mathrm{ref}}\|_L^2}{\|\phi_{\mathrm{ref}}\|_L^2} \tag{107}$$

where ϕ denotes ε^{in} or χ. The error (107) is evaluated independently at each of 20 stress levels in the test set $\Lambda \in [1.06, 1.47]$, distinct from the collocation points used during training.

5. Computational Validation

At the material point level and under prescribed uniaxial stress, the PINN is validated with illustrative parameters ($\sigma_{Y0} = 150$ MPa, $\Delta\sigma_Y = 50$ MPa, $\eta = 10^8$ s, $n = 3$, $\sigma_0 = 100$ MPa, $c = 5000$ MPa, $\varkappa = 100$, $\tau_{\text{rec}} = 10^6$ s; symbols defined in Table 1). Since the material point formulation involves no spatial discretisation, boundary conditions, or equilibrium residuals, the constitutive response is isolated in its entirety. The theoretical contributions — the arrest stability theorem, the three-regime classification, the acceleration effect — are properties of the constitutive equations themselves; their verification does not require a spatially resolved boundary value problem.

5.1. Test Configuration and Accuracy Metrics

The applied stress is parameterised by the load ratio $\Lambda = \sigma/\sigma_{Y0}$; this quantity and the normalised time $\bar{t} = t/\tau_h$ form the two-dimensional network input. Over the domain $(\Lambda, \bar{t}) \in [0.85, 1.50] \times [0, 5]$, the parametric PINN maps onto the output pair $\{\varepsilon^{\text{in}}, \chi\}$, so that the constitutive manifold is obtained over the full stress–time domain in a single training run. Quantitative error assessment is confined to $\Lambda \in [1.06, 1.47]$. The lower limit excludes the near-threshold band $\Lambda \in [1.00, 1.06]$, where the total accumulated inelastic strain is of order 10^{-8} — three to four orders of magnitude below the arrest-regime strains — so that the relative error metric is dominated by numerical noise rather than physics error.

Reference solutions for the coupled ODE system,

$$\frac{d\varepsilon^{\text{in}}}{dt} = \frac{1}{\eta}\left\langle \frac{\sigma - \chi - \sigma_Y(t)}{\sigma_0} \right\rangle^n, \qquad \frac{d\chi}{dt} = c\frac{d\varepsilon^{\text{in}}}{dt} - \varkappa\chi\left|\frac{d\varepsilon^{\text{in}}}{dt}\right| - \frac{\chi}{\tau_{\text{rec}}}, \tag{108}$$

are generated by the Radau IIA integrator with tolerances $r_{\text{tol}} = 10^{-10}$ and $a_{\text{tol}} = 10^{-13}$, evaluated on a uniform time grid of 2×10^3 points. For the purposes of error measurement, these solutions are treated as exact. The L^2 relative error quantifies the accuracy of the trained network separately for each output; the mean error across N_σ test levels is defined for each field, giving

$$\bar{\epsilon}^{\varepsilon^{\text{in}}}_{L^2} = \frac{1}{N_\sigma}\sum_{j=1}^{N_\sigma} \frac{\|\varepsilon^{\text{in}}_{\text{PINN}}\left(\Lambda_j, \cdot\right) - \varepsilon^{\text{in}}_{\text{ref}}\left(\Lambda_j, \cdot\right)\|^2_L}{\|\varepsilon^{\text{in}}_{\text{ref}}\left(\Lambda_j, \cdot\right)\|^2_L}, \tag{109}$$

$$\bar{\epsilon}^{\chi}_{L^2} = \frac{1}{N_\sigma}\sum_{j=1}^{N_\sigma} \frac{\|\chi_{\text{PINN}}\left(\Lambda_j, \cdot\right) - \chi_{\text{ref}}\left(\Lambda_j, \cdot\right)\|^2_L}{\max\left(\|\chi_{\text{ref}}\left(\Lambda_j, \cdot\right)\|^2_L,\, \chi_{\text{scale}} \times 10^{-2}\right)}, \tag{110}$$

where $N_\sigma = 20$ test levels, uniformly distributed over $\Lambda \in [1.06, 1.47]$, are distinct from the collocation points used during training. In (110), the denominator is taken as $\max\left(\|\chi_{\text{ref}}\|^2_L, \chi_{\text{scale}} \times 10^{-2}\right)$; without this floor, numerical noise would dominate the relative error when the reference back stress is near zero. The construction serves the same regularisation purpose as the ϵ floor in the general metric (107), but is scaled to the physical back-stress magnitude.

5.2. Training and Convergence

The two-output coupled system requires greater network capacity than a single-output formulation, since the nonlinear feedback $\varkappa\chi\left|\dot{\varepsilon}^{\text{in}}\right|$ in the Armstrong–Frederick equation creates a coupling that a narrow network cannot represent. Both outputs are accordingly normalised by their characteristic physical scales, with $\varepsilon_{\text{scale}} = (1/\eta) \cdot \left(\left(\sigma_{\text{mid}} - \sigma_{Y0}\right)/\sigma_0\right)^n \cdot \tau_h$ and $\chi_{\text{scale}} = c \cdot \varepsilon_{\text{scale}}$, where $\sigma_{\text{mid}} = \bar{\sigma}_{\text{mid}} \cdot \sigma_{Y0}$ uses the domain midpoint $\bar{\sigma}_{\text{mid}} = 1.175$ defined in (96).

Table 3 summarises the hyperparameter search space and the best values obtained. None of the trials improved upon the warm-start seed; the coupled problem therefore shares its optimal architecture with the simpler single-output variant. Convergence was most sensitive to the back-stress weight $\lambda_\chi = 10$. In trials with $\lambda_\chi < 3$, the back

Table 3: Hyperparameter search space for the coupled HPO study.

Hyperparameter	Search range	Best value
Network width n_h	$\{256, 512, 1024\}$	512
Network depth n_ℓ	$\{4, 6, 8\}$	6
Learning rate ℓ_r	$[10^{-4}, 10^{-3}]$	8.0×10^{-4}
Flow loss weight λ_{flow}	$[1, 500]$	1.0
Back-stress loss weight λ_χ	$[1, 100]$	10.0
Elastic weight λ_{el}	$[50, 500]$	300
Threshold weight λ_{th}	$[1, 30]$	10.0
Elastic collocation count N_{el}	$[500, 2000]$	1000
Threshold collocation count N_{th}	$[500, 2500]$	1800
$\tau_{\text{rec,eff}}$	$[5 \times 10^5, 5 \times 10^6]$ s	1.0×10^6 s

stress collapsed toward zero within 50,000 epochs, while $\lambda_\chi > 30$ caused the flow residual to be under-weighted and produced degraded ε^{in} accuracy.

Two design choices that had proved detrimental in the single-output study were equally problematic for the coupled formulation. Soft penalty enforcement of the initial conditions produced persistent IC violations; the output subtraction hard constraint (104) was again necessary. The progressive loss ramp over the first 30% of training was likewise retained, since activating the full coupled physics loss from epoch one caused early divergence.

The best configuration was retrained for 300,000 epochs using the SGDR schedule

$$T_{\text{restart}}^{(i)} = T_0 \cdot T_{\text{mult}}^i, \qquad T_0 = 20{,}000, \quad T_{\text{mult}} = 2 \tag{111}$$

giving restarts at epochs 20k, 60k, 140k, and 300k. The most pronounced improvement occurred at the 60k restart, where $\bar{\epsilon}_{L^2}^{\varepsilon^{\text{in}}}$ dropped from approximately 18% to 4.8% within 20,000 epochs; the learning rate reset destabilised a loss plateau that had persisted for 40,000 epochs. Selected training checkpoints are given in Table 4.

Table 4: Selected training checkpoints for the coupled ε^{in}–χ PINN.

Epoch	$\bar{\epsilon}_{L^2}^{\varepsilon^{\text{in}}}$	$\bar{\epsilon}_{L^2}^{\chi}$	Remark
50,000	20.59%	20.29%	—
100,000	4.84%	4.63%	Post-restart improvement
120,000	3.96%	3.29%	Second restart nadir
200,000	2.89%	3.27%	—
240,000	2.22%	2.81%	—
300,000	0.52%	0.41%	Final epoch

At the final export validation, conducted on 20 distinct test levels after training completion, the mean L^2 errors are

$$\bar{\epsilon}_{L^2}^{\varepsilon^{\text{in}}} = 0.30\%, \qquad \bar{\epsilon}_{L^2}^{\chi} = 0.24\% \tag{112}$$

The coupled formulation thus achieves a 14-fold improvement over the baseline single-output PINN (which solved only the flow rule without back-stress coupling), for which $\bar{\epsilon}_{L^2}^{\varepsilon^{\text{in}}} = 4.21\%$ under the same training duration and schedule. The improvement may be attributed to the additional physical structure provided by the back stress χ, since the Armstrong–Frederick equation constrains the solution manifold and thereby reduces the effective search space for the optimiser.

5.3. Accuracy and Constitutive Manifolds

The mean errors (112) conceal important structure across regimes. In the arrest regime ($\Lambda \in [1.06, 1.33]$), the mean errors are $\bar{\epsilon}_{L^2}^{\varepsilon^{\text{in}}} = 0.35\%$ and $\bar{\epsilon}_{L^2}^{\chi} = 0.30\%$; in the continuous flow regime ($\Lambda \in [1.33, 1.47]$), both errors fall to

0.01%. The near-threshold band ($\Lambda \in [1.00, 1.06]$) shows elevated relative errors that are numerical artefacts rather than physics errors, as discussed below.

In both regimes, the accuracy is sufficient to resolve the arrest time t^*, the final arrested strain $\varepsilon^{\text{in}}(t^*)$, and the long-time asymptotic behaviour in the continuous flow case, all to within the physical uncertainty of the material parameters.

The physical plausibility of the back-stress prediction was verified at three levels. For the continuous flow case ($\Lambda = 1.40$), the back stress approaches a quasi-steady equilibrium substantially below the Armstrong–Frederick saturation $c/\varkappa = 50$ MPa. In the coupled system, the growing back stress progressively reduces the effective stress $\Sigma_{\text{eq}} = \sigma - \chi - \sigma_Y(t)$, which in turn decelerates the inelastic strain rate. The equilibrium χ is therefore set by the self-consistent balance between hardening and the diminishing driving force. The reference ODE solver gives an equilibrium value of $\chi = 0.126$ MPa, and the PINN predicts $\chi = 0.126$ MPa — agreement to within 0.6% as $\bar{t} \to 5$. For the arrest case ($\Lambda = 1.10$), the back stress at $\bar{t} = 5$ is positive and non-zero — consistent with the slow static recovery at $\tau_{\text{rec}} = 10^6$ s — and the PINN value agrees with the reference to within 0.5%. In the elastic regime ($\Lambda = 0.95$), both outputs are suppressed to $O\left(10^{-6}\right)$ throughout.

The elevated near-threshold error ($\Lambda \in [1.00, 1.06]$) requires qualification. In this band, the total accumulated inelastic strain over the full simulation horizon is of order 10^{-8} — three to four orders of magnitude below the arrest-regime strains. The relative error metric divides by this near-zero reference norm; absolute prediction errors of order 10^{-9} accordingly produce large relative percentages despite being mechanically negligible.

For each stress level in the arrest regime, the predicted arrest time t^*_{PINN} is identified as the time at which the PINN strain rate first falls below 1% of its initial peak value. Comparison with the Radau reference solution shows agreement to within 5% across all arrest-regime test levels, with mean error 2%. The acceleration effect (88), wherein kinematic hardening reduces arrest time, is quantified by the ratio t^*/t^*_0. At the illustrative parameters, the reference ODE solutions give acceleration ratios in the range $t^*/t^*_0 \in [0.69, 0.88]$; kinematic hardening accordingly accelerates arrest by 12–31% depending on stress level. The applicability of this acceleration to the experimentally calibrated material system is discussed in Section 6. The PINN reproduces these ratios to within 5%.

Figure 9 shows the constitutive manifold over the $(\Lambda, \bar{t})$ domain, presenting the normalised inelastic strain $\varepsilon^{\text{in}}/\varepsilon^{\text{in}}_{\max}$ computed from the reference ODE solution at the illustrative parameters listed in Section 5. The three behavioural regimes derived in Section 3.1 are resolved without ambiguity. Regime I ($\Lambda < 1$) is identically flat at zero strain; Regime II ($1 < \Lambda < 1 + \Gamma$) shows initial flow that saturates at a finite arrested strain; and Regime III ($\Lambda > 1 + \Gamma$) exhibits monotonically increasing strain throughout the simulation horizon. The arrest boundary $t^*(\Lambda)$ traces a curve on the manifold surface, separating the arrested plateau from the actively flowing region. It follows that the three-regime classification of Section 3.1 is not restricted to the theoretical analysis but is directly present in the computed constitutive response. The PINN reproduces this manifold, including the arrest boundary location and the plateau heights, to within the L^2 errors reported above.

6. Experimental Calibration and Validation

In view of the sub-percent verification accuracy established in Section 5, the constitutive equations are now calibrated against experimental data to determine whether they represent the behaviour of a real material. The framework of Sections 2–3 is calibrated to AA7050-T6 aluminium alloy at 174 °C using data from the CABT. The calibration relies exclusively on the coupled ODE system (108) integrated by the Radau IIA method; no PINN is involved. Since Section 5 has shown that the PINN reproduces the ODE solution to within 0.30% (inelastic strain) and 0.24% (back stress), it follows that a PINN trained at the calibrated parameters would reproduce the experimental behaviour to within the sum of the ODE-to-experiment mismatch and the PINN-to-ODE error — the latter being negligible relative to the former.

6.1. Experimental Programme

The creep-ageing and back-stress test (CABT) is adopted as the sole experimental protocol. During the loading phase, a tensile load is applied and held at constant stress while strain is monitored continuously; the time-resolved inelastic strain histories so obtained are used for calibration. Upon unloading, the specimen strain is held constant by the testing machine, and the resulting stress evolution provides a direct measurement of the back stress. All tests were

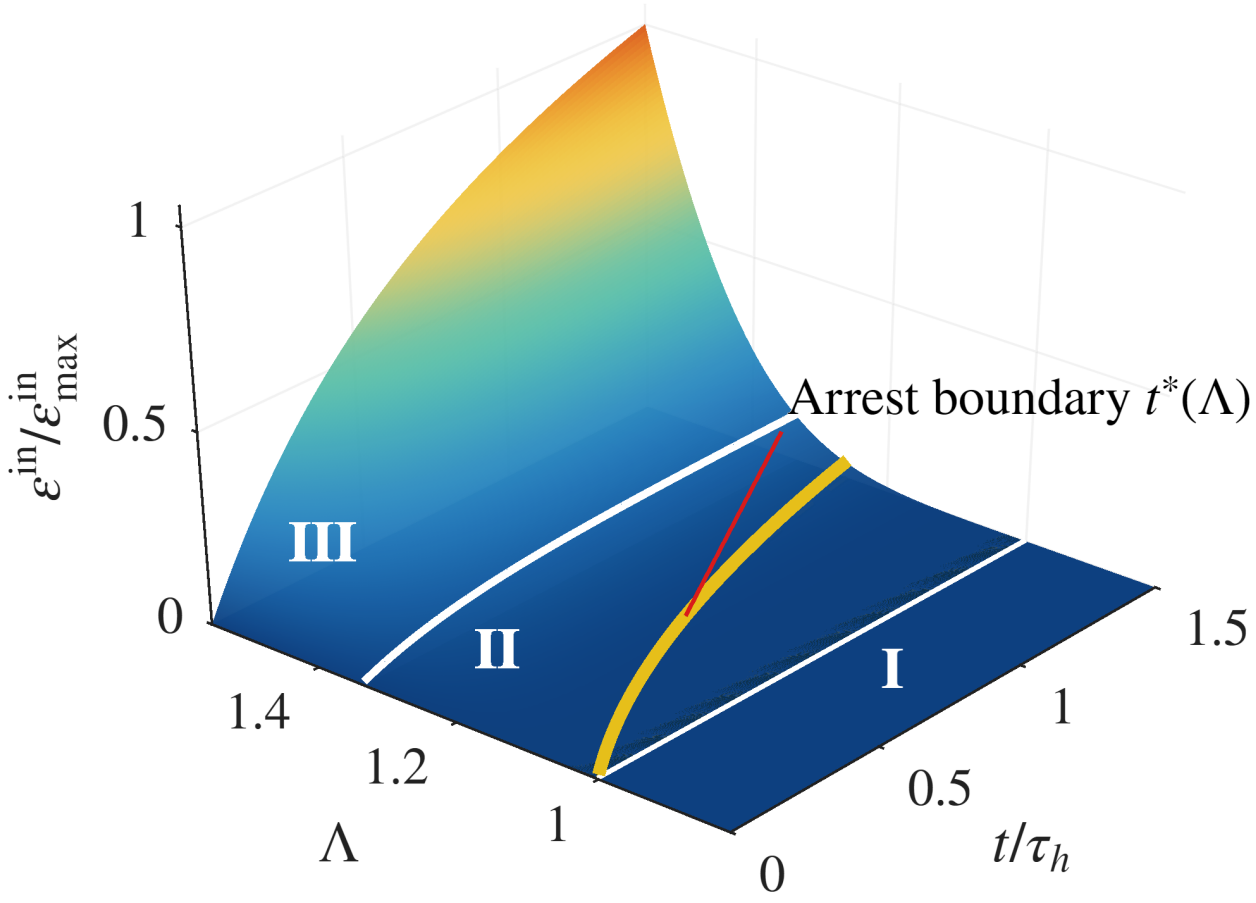

Figure 9: Constitutive manifold $\varepsilon^{\text{in}}/\varepsilon^{\text{in}}_{\text{max}}$ over the $(\Lambda, t/\tau_h)$ domain computed from the reference ODE solution at illustrative parameters (Section 5), with three-regime classification (I: elastic, II: arrested, III: continuous flow) and the arrest boundary $t^*(\Lambda)$ highlighted. Colour represents normalised inelastic strain magnitude.

conducted on an Instron 5584 testing machine equipped with a temperature chamber maintained at 174 ± 1 °C. Strain was measured with an Instron 2630-107 extensometer.

In each test, the specimen is loaded at 8 MPa/s to the target stress level and held at constant stress for a prescribed duration. The rapid loading rate minimises inelastic strain accumulation during the ramp, so that the creep holding phase begins with negligible pre-strain. Tests were conducted at three stress levels — 137.5, 150, and 162.5 MPa — for holding durations of 5 min, 10 min, 30 min, 1, 2, 4, 6, and 8 hours; each combination requires a separate specimen, because the test is destructive. For calibration of the creep response, only the 8-hour holding data at all three stress levels are used, since these provide the longest observation window over which the competitive hardening dynamics can be resolved. The inelastic strain $\varepsilon^{\text{in}}(t)$ is the difference between the measured total strain during the constant-stress holding phase and the elastic component σ/E, where $E = 65.2$ GPa denotes the Young's modulus as determined from the unloading slope.

The CABT is a testing technique developed by the present author to quantify the internal stresses responsible for anelastic recovery [87]. Existing methods for back-stress measurement — incremental unloading [2], strain transient dip [13], and stress change tests — determine the back stress at a single instant by perturbing the loading condition and observing the transient response. In the CABT, a specimen is crept at constant stress for a prescribed duration and then unloaded to zero stress, at which point the strain is held constant by the testing machine. Under this strain-constrained condition, the back stress manifests as a measurable stress that develops in the specimen and eventually saturates, giving a direct measurement of the back stress present at the end of the creep-ageing period.

The saturation back stress χ_{sat} is approximately independent of the applied stress level; it varies only with creep-ageing duration. This stress-independence is consistent with the Armstrong–Frederick kinematic hardening model adopted in Section 2, for which the theoretical saturation value $\chi_{\text{sat}} = c/\varkappa$ is a material constant. The data used for calibration are the discrete saturation back-stress values $\chi_{\max}\left(t_{\text{creep}}\right)$ extracted from each test, which together trace the evolution of back stress with creep-ageing time. The complete test sequences at 150 MPa for all hold durations are displayed as a three-dimensional waterfall in Figure 10.

Two features of the CABT data displayed in Figure 10 directly constrain the constitutive model. The back-stress rise curves (orange segments) show an initial rapid increase followed by saturation at a plateau value that grows with hold duration up to approximately 4 h, beyond which further creep-ageing produces no additional back stress. This saturation corresponds to the Armstrong–Frederick dynamic recovery term $(-\varkappa\chi\dot{p})$ in Eq. (30), which limits the back stress to $\chi_{\text{sat}} = c/\varkappa$ regardless of the total accumulated strain. In addition, the plateau values are approximately independent of the applied stress level — a feature confirmed across all three stress levels in the full test matrix — consistent with the theoretical prediction that χ_{sat} is a material constant rather than a function of the applied loading.

6.2. Calibration Procedure

The uniaxial specialisation of the constitutive framework involves seven fitted parameters — σ_{Y0}, $\Delta\sigma_Y$, τ_h, η, n, c, and $\varkappa$ — and two fixed constants: the reference stress $\sigma_0 = 1$ MPa (a normalisation constant degenerate with η) and the static recovery time $\tau_{\text{rec}} = 10^6$ s.

The reference stress σ_0 cannot be determined independently, because the flow rule contains the compound quantity $\eta \cdot \sigma_0^n$; only this product is identifiable from data. The static recovery time τ_{rec} significantly exceeds the observation window, and the CABT data show no visible back-stress decay after saturation; τ_{rec} is therefore fixed at 10^6 s throughout.

The experimental data impose physical constraints that restrict the parameter space before fitting begins. At $t = 0$, the back stress is zero and the threshold stress is at its initial value σ_{Y0}. The flow rule then reduces to $\dot{\varepsilon}^{\text{in}}(0) = (1/\eta)\left[(\sigma - \sigma_{Y0})/\sigma_0\right]^n$, and the ratio of any two initial rates eliminates η, giving

$$\frac{\dot{\varepsilon}_0^{\text{in}}(\sigma_1)}{\dot{\varepsilon}_0^{\text{in}}(\sigma_2)} = \left(\frac{\sigma_1 - \sigma_{Y0}}{\sigma_2 - \sigma_{Y0}}\right)^n \tag{113}$$

Two such ratios from three stress levels furnish two equations in two unknowns (n, σ_{Y0}). Once these are determined, η follows from any single initial rate. The saturation back stress $\chi_{\text{sat}} \approx c/\varkappa$ is read directly from the plateau of the CABT data, so that the ratio $c/\varkappa$ is constrained before the full optimisation begins.

The seven parameters are fitted simultaneously to both datasets by nonlinear least-squares minimisation (Levenberg–Marquardt via MATLAB `lsqnonlin`) of the combined cost function

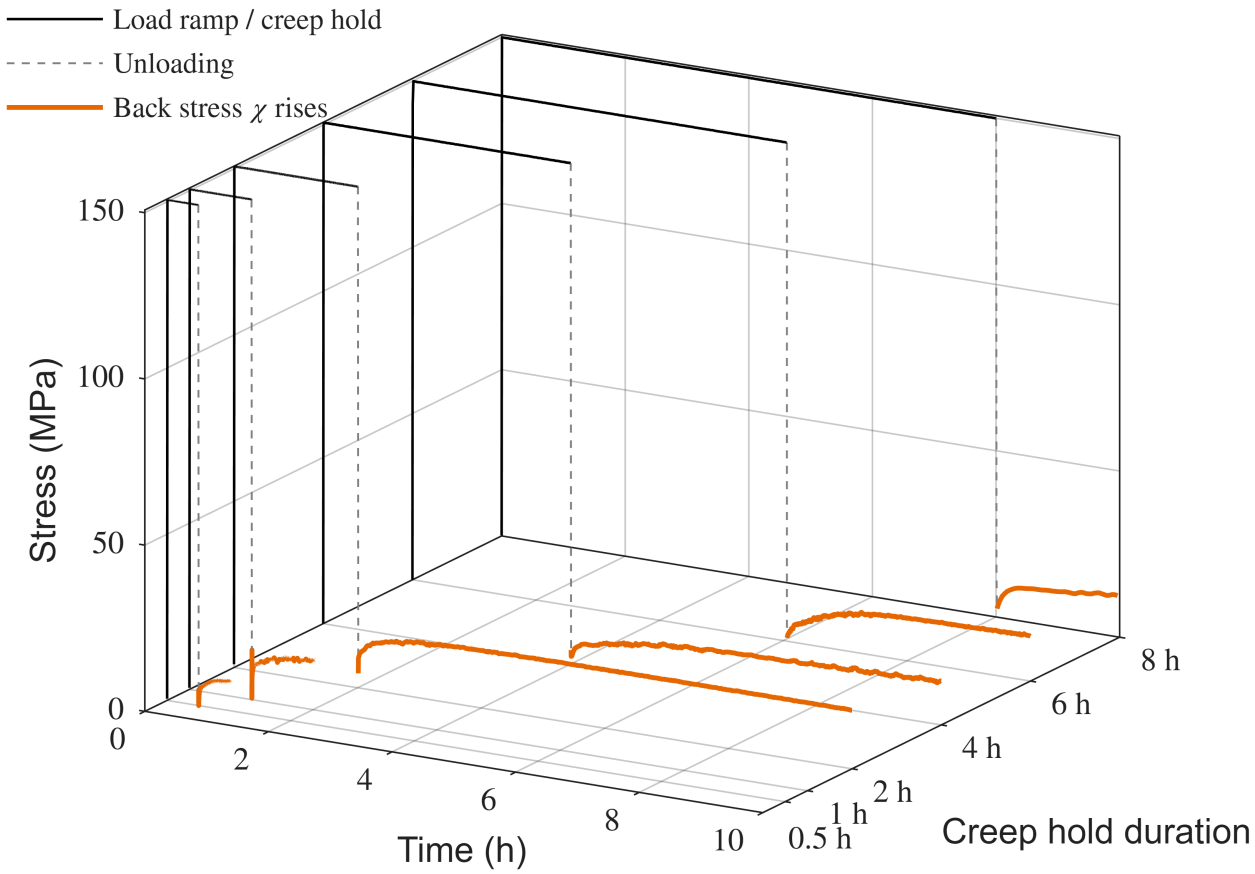

Figure 10: Three-dimensional waterfall of CABT raw data for AA7050-T6 at 150 MPa and 174 °C. Each curve shows the complete test sequence — load ramp (black), unloading (dashed), and back-stress rise phase (orange) — for creep hold durations from 0.5 h to 8 h. Back stress increases with hold duration and saturates beyond approximately 4 h.

$$\mathcal{R}(\mathbf{p}) = \sum_{k=1}^{3} \left\| \frac{\varepsilon^{\mathrm{in}}_{\mathrm{model}}(t;\sigma_k,\mathbf{p}) - \varepsilon^{\mathrm{in}}_{\mathrm{exp}}(t;\sigma_k)}{\varepsilon^{\mathrm{in,max}}_{\mathrm{exp}}(\sigma_k)} \right\|^2 + w_\chi \sum_{k=1}^{3} \sum_{j} \left(\frac{\chi_{\mathrm{model}}\left(t_j;\sigma_k,\mathbf{p}\right) - \chi_{\mathrm{CABT}}\left(t_j;\sigma_k\right)}{\chi_{\mathrm{sat}}} \right)^2 \tag{114}$$

where $\mathbf{p} = (\sigma_{Y0}, \Delta\sigma_Y, \tau_h, \eta, n, c, \varkappa)$, the first sum runs over the three creep stress levels with continuous time series, and the second sum runs over the discrete CABT saturation points. The forward model integrates the coupled ODE system (108) with `ode15s` at tolerance 10^{-10}. Each dataset is normalised by its characteristic scale — the maximum observed inelastic strain for the creep data, the saturation back stress for the CABT data — and the weight w_χ is chosen so that neither dataset dominates the combined objective. The solution is verified by initialising the optimiser from three independent starting points, all of which converge to the same parameter values within solver tolerance.

6.3. Calibration Results

The calibrated parameters are listed in Table 5.

Table 5: Calibrated material parameters for AA7050-T6 at 174 °C.

Parameter	Symbol	Value	Unit
Initial threshold stress	σ_{Y0}	0 (calibrated; fixed at 0)	MPa
Threshold increment	$\Delta\sigma_Y$	86.7	MPa
Ageing time constant	τ_h	3552	s
Viscous resistance	η	5.42×10^9	s
Stress exponent	n	1.39	—
Back-stress modulus	c	7.18×10^4	MPa
Dynamic recovery coefficient	$\varkappa$	4756	—
Reference stress (fixed)	σ_0	1	MPa
Static recovery time (fixed)	τ_{rec}	10^6	s

The calibrated model is compared against the experimental inelastic strain histories in Figure 11(a). The model reproduces the primary creep deceleration and the transition toward secondary creep at all three stress levels with a single parameter set. The mean RMSE across the three stress levels is 0.004% strain. The stress sensitivity is also reproduced, since the creep rate increases with applied stress in a manner consistent with the power-law flow rule. A slight over-prediction at 162.5 MPa in the late-time region (beyond 5 h) reflects the single-kinetics limitation of the exponential ageing function (20); the real precipitation process involves an early fast phase and a later slow phase that one time constant cannot resolve.

The back-stress evolution predicted by the calibrated model is compared against the discrete CABT measurements in Figure 11(b). The model recovers both the rapid build-up during primary creep and the saturation toward $\chi_{\mathrm{sat}} = c/\varkappa = 15.1$ MPa. The approximate stress-independence of χ_{sat} is likewise recovered; the three stress levels converge to similar saturation values, consistent with the Armstrong–Frederick structure in which χ_{sat} is a material constant. The mean RMSE across the three stress levels is 1.1 MPa. The CABT data constrain the ratio $c/\varkappa$ but not the individual values; the individual magnitudes of c and $\varkappa$ are determined primarily by the rate of back-stress build-up observed in the creep data. The agreement between the model and the CABT saturation data therefore constitutes an independent check on the coupling between the kinematic hardening dynamics and the viscoplastic flow rule. A PINN retrained at the calibrated parameters (Table 5) reproduced the Radau IIA reference solutions to mean L^2 errors of 0.03% ($\varepsilon^{\mathrm{in}}$) and 0.02% ($\chi$); the predictions are overlaid in Figure 11(b).

6.4. Discussion

The seven-parameter calibration produces a constitutive model that simultaneously reproduces two independent experimental datasets — creep strain histories and back-stress evolution (CABT) — at three stress levels with a single parameter set. Several observations merit discussion.

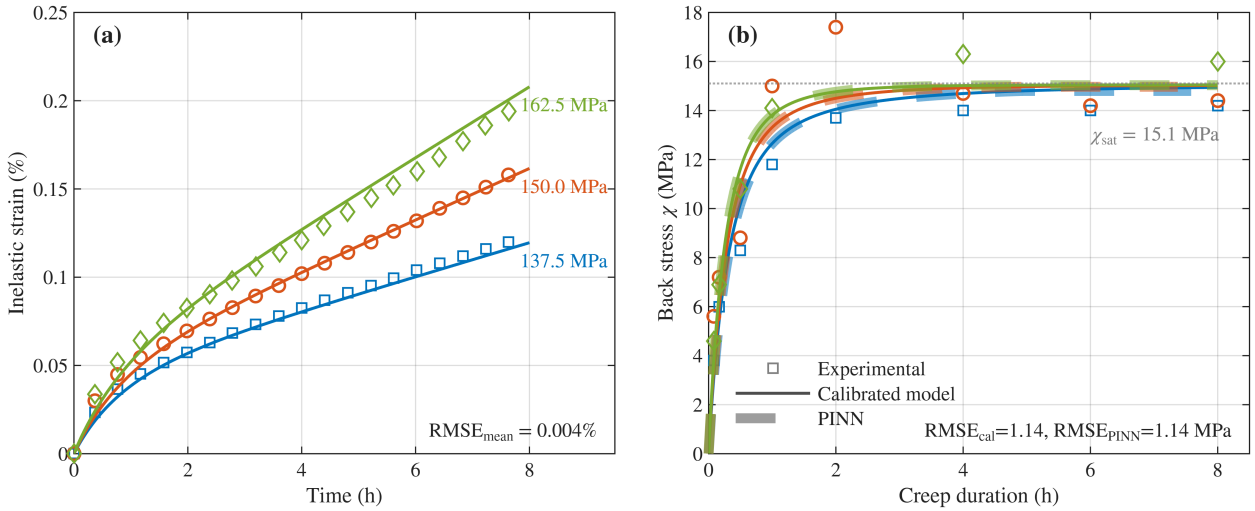

Figure 11: Experimental validation of the calibrated constitutive model for AA7050-T6 at 174 °C: (a) inelastic creep strain histories at 137.5, 150, and 162.5 MPa with calibrated ODE model (solid lines) and experimental data (markers); (b) back-stress evolution from CABT measurements (markers) with calibrated ODE model (solid) and PINN predictions at calibrated parameters (dashed) at three stress levels, with $\chi_{sat} \approx 15.1$ MPa.

The CABT provides the only direct experimental access to the back stress in this framework. Without it, the parameters c and $\varkappa$ would be determined indirectly from the curvature of the creep curves — a numerically ill-conditioned procedure, since χ enters the flow rule as a correction to the applied stress and its individual effect is difficult to distinguish from changes in σ_{Y0} or η; the CABT data accordingly resolve this ambiguity through an independent measurement that constrains the back-stress subsystem.

The calibrated $\sigma_{Y0} = 0$ is the threshold stress for inelastic flow activation in the Perzyna flow rule — not the tensile yield strength measured by a 0.2% offset convention. The two quantities are related but distinct; the tensile yield strength includes rate effects, strain hardening, and the offset definition, while σ_{Y0} is the stress below which the Macaulay bracket (27) is identically zero and no inelastic flow occurs. This distinction bears on any comparison of the present calibration with values reported in the age-hardening literature.

The calibrated value $\sigma_{Y0} = 0$ places this material in the degenerate case addressed by the Remark in Section 3.1, where the dimensionless parameters Λ and Γ are undefined and the asymptotic threshold $\sigma_{Y\infty} = \Delta\sigma_Y = 86.7$ MPa serves as the normalising stress. With $\sigma_{Y0} = 0$, the initial-rate ratio (113) simplifies to $(\sigma_1/\sigma_2)^n$, and the stress exponent n is accordingly determined directly from the ratio of initial creep rates at any two stress levels without requiring prior estimation of the threshold stress.

The regime classification reduces in parallel. The three-regime map collapses to two regimes — continuous flow ($\Lambda_\infty > 1$) and eventual arrest ($\Lambda_\infty < 1$) — with no purely elastic regime, because every nonzero stress exceeds the zero initial threshold. At 137.5 MPa ($\Lambda_\infty = 1.59$), 150 MPa ($\Lambda_\infty = 1.73$), and 162.5 MPa ($\Lambda_\infty = 1.87$), all three experimental stress levels lie well above the asymptotic threshold and are therefore in the continuous flow regime — consistent with the experimental creep curves, which show sustained creep throughout the 8-hour window without the strain plateau that would indicate arrest.

The present calibration contains no arrest-regime data, because all three stress levels lie well into the continuous flow regime ($\Lambda_\infty > 1.5$). Experimental validation of the arrest transition predicted by the framework (Sections 3.1–3.2) would require applied stresses below $\sigma_{Y\infty} = 86.7$ MPa — a regime accessible through stress relaxation or low-stress creep tests. Such experiments offer a natural direction for future work.

For the same reason, the kinematic hardening acceleration effect derived in Section 3.3 is not directly observable in the present dataset. At the illustrative parameters of Section 5, the acceleration ratios lie in the range $t^*/t_0^* \in [0.69, 0.88]$, corresponding to a 12–31% reduction in arrest time; evaluating the corresponding ratios at the calibrated AA7050 parameters would require applied stresses below $\sigma_{Y\infty} = 86.7$ MPa, which lie outside the present experimental design.

The one-sided Macaulay bracket adopted in this work permits only forward flow. The anelastic recovery observed

after unloading — in which strain decreases under zero applied stress — requires a signed flow rule capable of reverse inelastic flow driven by the back stress. The present calibration accordingly uses only the constant-stress holding phase. The static recovery timescale τ_{rec} is likewise unidentifiable from the present dataset; its determination requires either much longer observation windows or controlled reverse-loading experiments.

7. Conclusions

A constitutive framework has been developed in which the threshold stress is governed by first-order ageing kinetics and evolves with physical time independently of the accumulated inelastic strain. The back stress follows a modified Armstrong–Frederick evolution with static recovery, and the two subsystems are coupled through the Perzyna-type flow rule. Thermodynamic admissibility has been established for all admissible processes through the Clausius–Duhem inequality (Section 2.4).

The competition between time-driven threshold evolution and strain-driven kinematic hardening gives rise to three behavioural regimes — elastic, flow arrest, and continuous flow — classified by the dimensionless load ratio Λ and hardening capacity Γ (Section 3.1, Figure 5). A constructive Lyapunov function (Eqs. (72)–(76)) establishes that flow arrest is asymptotically stable; to the author's knowledge, no comparable stability proof at the material-point level has been given in the viscoplastic creep literature. An analytical bound on the kinematic hardening acceleration effect (Eq. (88)) predicts that back-stress development reduces arrest time by 12–31% at the illustrative parameters of Section 5. At the calibrated AA7050 parameters, however, all experimental stress levels lie in the continuous flow regime ($\Lambda_\infty > 1.5$); the arrest transition itself accordingly awaits experimental confirmation at lower stresses (Section 6.4).

The parametric PINN formulated in Section 4 approximates the coupled constitutive response over the stress–time domain in a single training run. At the illustrative parameters, the trained network achieves mean L^2 errors of 0.30% for inelastic strain and 0.24% for back stress against Radau IIA reference solutions (Section 5, Figure 9), and reproduces the elastic, arrest, and continuous flow regimes without regime-specific tuning. At the calibrated AA7050 parameters, a retrained PINN achieves 0.03% and 0.02% respectively (Section 6.3, Figure 11). The smooth Macaulay bracket approximation with curriculum learning, together with hard initial condition enforcement through output subtraction, proved necessary for stable convergence; physical output scaling is required because raw network outputs and physical field magnitudes differ by seven orders of magnitude.

The constitutive framework has been calibrated to AA7050-T6 aluminium alloy at 174 °C using data from the creep-ageing and back-stress test (CABT) — a measurement technique developed by the present author — whose loading phase furnishes inelastic strain histories and whose post-unloading phase yields direct back-stress measurements. A seven-parameter calibration simultaneously reproduces both datasets at three stress levels with mean RMSE of 0.004% strain (creep phase) and 1.1 MPa (back-stress phase). The independent agreement between the model and the CABT saturation data provides a direct check on the coupling between the kinematic hardening dynamics and the viscoplastic flow rule.

The present formulation adopts a one-sided Macaulay bracket that admits only forward flow; extension to a signed flow rule would permit prediction of anelastic recovery and the Bauschinger effect under load reversal. The parametric PINN is differentiable with respect to its inputs (stress and time), and accordingly admits further extension. Incorporating material parameters into the network input space would furnish a fully differentiable surrogate for gradient-based inverse parameter identification from sparse experimental data; Bayesian treatment of the same framework would provide uncertainty quantification for the calibrated parameters. The arrest transition predicted by the framework ($\Lambda_\infty < 1$) has not been validated experimentally at the present stress levels; low-stress creep or stress relaxation tests below $\sigma_{\gamma\infty} = 86.7$ MPa would constitute a direct experimental test of the arrest prediction. These extensions lie beyond the scope of the present work.

Acknowledgments

This research was funded by the National Science and Technology Council (NSTC), Taiwan, under Grant No. 112-2221-E-027-118-. The experimental data reported in Section 6 were obtained at the Department of Mechanical Engineering, Imperial College London, as part of the author's doctoral research under the supervision of Prof. Jianguo Lin.

References

[1] Zener, C., *Elasticity and anelasticity of metals*. 1948, Chicago, Illinois: University of Chicago Press.

[2] Gibeling, J.C. and W.D. Nix, *The description of elevated temperature deformation in terms of threshold stresses and back stresses: A review.* Materials Science and Engineering, 1980. **45**(2): p. 123–135.

[3] Sinha, N.K., *Viscous and delayed-elastic deformation during primary creep-using strain relaxation and recovery test.* Scripta Materialia, 2003. **48**(10): p. 1507–1512.

[4] Sinha, N.K. and S. Sinha, *High-temperature yield strength and its dependence on primary creep and recovery.* Materials Science and Engineering: A, 2011. **528**(16-17): p. 5366–5378.

[5] Wei, Y., A.F. Bower, and H. Gao, *Recoverable creep deformation due to heterogeneous grain-boundary diffusion and sliding.* Scripta Materialia, 2007. **57**(10): p. 933–936.

[6] Gibeling, J.C. and W.D. Nix, *Observations of anelastic backflow following stress reductions during creep of pure metals.* Acta Metallurgica, 1981. **29**(10): p. 1769–1784.

[7] Mughrabi, H., *Dislocation wall and cell structures and long-range internal stresses in deformed metal crystals.* Acta Metallurgica, 1983. **31**(9): p. 1367–1379.

[8] Zelenika, A., et al., *Observing formation and evolution of dislocation cells during plastic deformation.* Scientific Reports, 2025. **15**(1): p. 8655.

[9] Li, D. and R.H. Wagoner, *The nature of yielding and anelasticity in metals.* Acta Materialia, 2021. **206**: p. 116625.

[10] Čadek, J., *The back stress concept in power law creep of metals: A review.* Materials Science and Engineering, 1987. **94**: p. 79–92.

[11] Kassner, M.E., P. Geantil, and L.E. Levine, *Long range internal stresses in single-phase crystalline materials.* International Journal of Plasticity, 2013. **45**: p. 44–60.

[12] Zhu, Y. and X. Wu, *Perspective on hetero-deformation induced (HDI) hardening and back stress.* Materials Research Letters, 2019. **7**(10): p. 393–398.

[13] Ahlquist, C.N. and W.D. Nix, *The measurement of internal stresses during creep of al and Al-Mg alloys.* Acta Metallurgica, 1971. **19**(4): p. 373–385.

[14] Chen, R., et al., *Hetero-deformation induced (HDI) stress measurement from the plastic dissipation in the hysteresis loops.* Materials Research Letters, 2025. **13**(3): p. 248–255.

[15] Chen, B., et al., *A review of the changes of internal state related to high temperature creep of polycrystalline metals and alloys.* International Materials Reviews, 2015. **60**(1): p. 1–29.

[16] Garofalo, F., *Fundamentals of Creep and Creep-Rupture in Metals*. 1965, New York: Macmillan.

[17] Lin, J., et al., *Development of dislocation-based unified material model for simulating microstructure evolution in multipass hot rolling.* Philosophical Magazine, 2005. **85**(18): p. 1967–1987.

[18] Perzyna, P., *Fundamental Problems in Viscoplasticity*, in *Advances in Applied Mechanics*, G.G. Chernyi, et al., Editors. 1966, Elsevier. p. 243–377.

[19] Chaboche, J.L., *Viscoplastic constitutive equations for the description of cyclic and anisotropic behaviour of metals.* Bulletin de l'Académie Polonaise des Sciences, Série des Sciences Techniques, 1977. **25**(1): p. 39–48.

[20] Chaboche, J.L., *A review of some plasticity and viscoplasticity constitutive theories.* International Journal of Plasticity, 2008. **24**(10): p. 1642–1693.

[21] Chaboche, J.L., *Time-independent constitutive theories for cyclic plasticity.* International Journal of Plasticity, 1986. **2**(2): p. 149–188.

[22] Meyer, K.A. and J. Ahlström, *The role of accumulated plasticity on yield surface evolution in pearlitic steel.* Mechanics of Materials, 2023. **179**: p. 104582.

[23] Li, Y., Z. Shi, and J. Lin, *Experimental investigation and modelling of yield strength and work hardening behaviour of artificially aged Al-Cu-Li alloy.* Materials & Design, 2019. **183**: p. 108121.

[24] Ma, Z., et al., *Stress-level-dependency and bimodal precipitation behaviors during creep ageing of Al-Cu alloy: Experiments and modeling.* International Journal of Plasticity, 2018. **110**: p. 183–201.

[25] Wang, X., et al., *Improved creep behaviour for a high strength Al-Li alloy in creep age forming: Experimental studies and constitutive modelling.* International Journal of Plasticity, 2022. **159**: p. 103447.

[26] Machado Alves da Fonseca, F., et al., *Long-Term Stability and Resulting Viscoplastic Behavior of Alloy 625 at 700 °C.* Metallurgical and Materials Transactions A, 2025.

[27] Li, Y., et al., *Constitutive modelling of coupled creep deformation and age hardening behavior of aluminum alloys under various thermal and mechanical loadings.* Journal of Materials Research and Technology, 2023. **25**: p. 333–353.

[28] Lei, M., et al., *A multi-mechanism coupled creep constitutive modeling with computable parameters.* International Journal of Plasticity, 2025. **195**: p. 104510.

[29] Bartošák, M. and J. Horváth, *A continuum damage coupled unified viscoplastic model for simulating the mechanical behaviour of a ductile cast iron under isothermal low-cycle fatigue, fatigue-creep and creep loading.* International Journal of Plasticity, 2024. **173**: p. 103868.

[30] Prager, W., *A New Method of Analyzing Stresses and Strains in Work-Hardening Plastic Solids.* Journal of Applied Mechanics, 1956. **23**(4): p. 493–496.

[31] Lemaitre, J. and J.-L. Chaboche, *Mechanics of Solid Materials*. 1990, Cambridge: Cambridge University Press.

[32] Khan, A.S. and S. Huang, *Experimental and theoretical study of mechanical behavior of 1100 aluminum in the strain rate range 10–5–104s–1.* International Journal of Plasticity, 1992. **8**(4): p. 397–424.

[33] Dafalias, Y.F. and E.P. Popov, *A model of nonlinearly hardening materials for complex loading.* Acta Mechanica, 1975. **21**(3): p. 173–192.

[34] Frederick, C.O. and P.J. Armstrong, *A mathematical representation of the multiaxial Bauschinger effect.* Materials at High Temperatures, 2007. **24**(1): p. 1–26.

[35] Chaboche, J.L., *On some modifications of kinematic hardening to improve the description of ratchetting effects.* International Journal of Plasticity, 1991. **7**(7): p. 661–678.

[36] Chaboche, J.L., *Constitutive equations for cyclic plasticity and cyclic viscoplasticity.* International Journal of Plasticity, 1989. **5**(3): p. 247–302.

[37] Ohno, N. and J.D. Wang, *Kinematic hardening rules with critical state of dynamic recovery, part I: formulation and basic features for ratchetting behavior.* International Journal of Plasticity, 1993. **9**(3): p. 375–390.

[38] Ohno, N. and J.D. Wang, *Kinematic hardening rules with critical state of dynamic recovery, part II: Application to experiments of ratchetting behavior.* International Journal of Plasticity, 1993. **9**(3): p. 391–403.

[39] Ohno, N., et al., *Modeling of cyclic hardening and evaluation of plastic strain range in the presence of pre-loading and ratcheting.* International Journal of Plasticity, 2021. **145**: p. 103074.

[40] Ning, Z., et al., *A kinematic hardening constitutive model for anomalous multiaxial ratcheting behaviors of zirconium alloy tubes under combined cyclic axial load and internal pressure at 648 K.* International Journal of Plasticity, 2025. **184**: p. 104202.

[41] Zirkle, T., T. Zhu, and D.L. McDowell, *Micromechanical crystal plasticity back stress evolution within FCC dislocation substructure.* International Journal of Plasticity, 2021. **146**: p. 103082.

[42] Evers, L.P., W.A.M. Brekelmans, and M.G.D. Geers, *Non-local crystal plasticity model with intrinsic SSD and GND effects.* Journal of the Mechanics and Physics of Solids, 2004. **52**(10): p. 2379–2401.

[43] Zhang, X., et al., *Geometrically necessary dislocations and related kinematic hardening in gradient grained materials: A nonlocal crystal plasticity study.* International Journal of Plasticity, 2023. **163**: p. 103553.

[44] Ispánovity, P.D., S. Papanikolaou, and I. Groma, *Emergence and role of dipolar dislocation patterns in discrete and continuum formulations of plasticity.* Physical Review B, 2020. **101**(2): p. 024105.

[45] Qin, J., B. Holmedal, and O.S. Hopperstad, *A combined isotropic, kinematic and distortional hardening model for aluminum and steels under complex strain-path changes.* International Journal of Plasticity, 2018. **101**: p. 156–169.

[46] Xu, H., et al., *A New Stored Energy Model Based on Plastic Work of Back Stress during Cyclic Loading in Polycrystalline Metal.* Materials, 2022. **15**(15): p. 5267.

[47] Coleman, B.D. and M.E. Gurtin, *Thermodynamics with Internal State Variables.* Journal of Chemical Physics, 1967. **47**: p. 597–613.

[48] McDowell, D.L. and Z.-K. Liu, *Hierarchical Nonequilibrium Thermodynamics of Thermally Activated Dislocation Plasticity of Metals and Alloys.* International Journal of Plasticity, 2025. **188**: p. 104303.

[49] McDowell, D.L., *Nonequilibrium thermodynamics, kinetics, and self-organization of dislocation avalanche plasticity.* International Journal of Plasticity, 2025. **195**: p. 104504.

[50] Oppermann, P., R. Denzer, and A. Menzel, *A thermo-viscoplasticity model for metals over wide temperature ranges- application to case hardening steel.* Computational Mechanics, 2022. **69**(2): p. 541–563.

[51] Zhu, Y., et al., *Thermo-mechanically coupled cyclic elasto-viscoplastic constitutive model of metals: Theory and application.* International Journal of Plasticity, 2016. **79**: p. 111–152.

[52] Ren, Z., et al., *Nonlinear Mixed Hardening Constitutive Model Considering Coupling Damage Under Multiaxial Non-proportional Loading Conditions.* Iranian Journal of Science and Technology, Transactions of Mechanical Engineering, 2025. **49**(1): p. 299–313.

[53] Zhan, L., J. Lin, and T.A. Dean, *A review of the development of creep age forming: Experimentation, modelling and applications.* International Journal of Machine Tools and Manufacture, 2011. **51**(1): p. 1–17.

[54] Yang, Y.-L., et al., *Predictive modelling of creep age forming parameters using artificial neural networks.* Discover Applied Sciences, 2025. **7**(8).

[55] Wang, X., Z. Shi, and J. Lin, *A generalised framework for modelling anisotropic creep-ageing deformation and strength evolution of 2xxx aluminium alloys.* International Journal of Plasticity, 2024. **182**: p. 104114.

[56] Bignon, M., et al., *Interactions between plastic deformation and precipitation in Aluminium alloys: A crystal plasticity model.* Acta Materialia, 2023. **247**: p. 118735.

[57] Yang, J., et al., *Superposed hardening from precipitates and dislocations enhances strength-ductility balance in Al-Cu alloy.* International Journal of Plasticity, 2022. **158**: p. 103413.

[58] Li, Y., et al., *A unified constitutive model for asymmetric tension and compression creep-ageing behaviour of naturally aged Al-Cu-Li alloy.* International Journal of Plasticity, 2017. **89**: p. 130–149.

[59] Zheng, J.-H., et al., *A novel constitutive model for multi-step stress relaxation ageing of a pre-strained 7xxx series alloy.* International Journal of Plasticity, 2018. **106**: p. 31–47.

[60] Borbély, A., W. Blum, and T. Ungár, *On the relaxation of the long-range internal stresses of deformed copper upon unloading.* Materials Science and Engineering: A, 2000. **276**(1–2): p. 186–194.

[61] Deschamps, A. and Y. Brechet, *Influence of predeformation and ageing of an Al–Zn–Mg alloy—II. Modeling of precipitation kinetics and yield stress.* Acta Materialia, 1998. **47**(1): p. 293–305.

[62] Seidman, D.N., E.A. Marquis, and D.C. Dunand, *Precipitation strengthening at ambient and elevated temperatures of heat-treatable Al(Sc) alloys.* Acta Materialia, 2002. **50**(16): p. 4021–4035.

[63] Wagoner, R.H., H. Lim, and M.-G. Lee, *Advanced Issues in springback.* International Journal of Plasticity, 2013. **45**: p. 3–20.

[64] Karniadakis, G.E., et al., *Physics-informed machine learning.* Nature Reviews Physics, 2021. **3**(6): p. 422–440.

[65] Flaschel, M., S. Kumar, and L. De Lorenzis, *Unsupervised discovery of interpretable hyperelastic constitutive laws.* Computer Methods in Applied Mechanics and Engineering, 2021. **381**: p. 113852.

[66] Mozaffar, M., et al., *Deep learning predicts path-dependent plasticity.* Proceedings of the National Academy of Sciences, 2019. **116**(52): p. 26414–26420.

[67] Dornheim, J., et al., *Neural Networks for Constitutive Modeling: From Universal Function Approximators to Advanced Models and the Integration of Physics.* Archives of Computational Methods in Engineering, 2024. **31**(2): p. 1097–1127.

[68] Fuhg, J.N., et al., *A Review on Data-Driven Constitutive Laws for Solids.* Archives of Computational Methods in Engineering, 2025. **32**(3): p. 1841–1883.

[69] Jordan, B. and D. Mohr, *Training of a physics-based thermo-viscoplasticity model on big data for polypropylene.* International Journal of Plasticity, 2025. **184**: p. 104179.

[70] Raissi, M., P. Perdikaris, and G.E. Karniadakis, *Physics-informed neural networks: A deep learning framework for solving forward and inverse problems involving nonlinear partial differential equations.* Journal of Computational Physics, 2019. **378**: p. 686–707.

[71] Raissi, M., A. Yazdani, and G.E. Karniadakis, *Hidden fluid mechanics: Learning velocity and pressure fields from flow visualizations.* Science, 2020. **367**(6481): p. 1026–1030.

[72] Masi, F., et al., *Thermodynamics-based Artificial Neural Networks for constitutive modeling.* Journal of the Mechanics and Physics of Solids, 2021. **147**: p. 104277.

[73] Masi, F. and I. Stefanou, *Multiscale modeling of inelastic materials with Thermodynamics-based Artificial Neural Networks (TANN).* Computer Methods in Applied Mechanics and Engineering, 2022. **398**: p. 115190.

[74] Eghtesad, A., et al., *NN-EVP: A physics informed neural network-based elasto-viscoplastic framework for predictions of grain size-aware flow response.* International Journal of Plasticity, 2024. **181**.

[75] Yu, Z., et al., *Unified prediction of uniaxial ratcheting deformation at elevated temperatures with physics-informed multimodal network.* International Journal of Plasticity, 2025. **187**: p. 104275.

[76] Keshavarz, S., et al., *Advancing material simulations: Physics-Informed Neural Networks and Object-Oriented Crystal Plasticity Finite Element Methods.* International Journal of Plasticity, 2025. **185**: p. 104221.

[77] Niu, S., et al., *Modeling finite-strain plasticity using physics-informed neural network and assessment of the network performance.* Journal of the Mechanics and Physics of Solids, 2023. **172**: p. 105177.

[78] Maia, M.A., et al., *Physically recurrent neural networks for path-dependent heterogeneous materials: Embedding constitutive models in a data-driven surrogate.* Computer Methods in Applied Mechanics and Engineering, 2023. **407**: p. 115934.

[79] Vlassis, N.N. and W. Sun, *Sobolev training of thermodynamic-informed neural networks for interpretable elasto-plasticity models with level set hardening.* Computer Methods in Applied Mechanics and Engineering, 2021. **377**: p. 113695.

[80] Lai, Z., L. Zhao, and Q. Shao, *LENNs: Locally Enhanced Neural Networks for High-Fidelity Modeling in Solid Mechanics.* arXiv preprint arXiv:2510.18565, 2025.

[81] Gorji, M.B., et al., *On the potential of recurrent neural networks for modeling path dependent plasticity.* Journal of the Mechanics and Physics of Solids, 2020. **143**: p. 103972.

[82] Bonatti, C., B. Berisha, and D. Mohr, *From CP-FFT to CP-RNN: Recurrent neural network surrogate model of crystal plasticity.* International Journal of Plasticity, 2022. **158**: p. 103430.

[83] Heidenreich, J.N. and D. Mohr, *Extended minimal state cells (EMSC): Self-consistent recurrent neural networks for rate- and temperature dependent plasticity.* International Journal of Plasticity, 2025. **188**: p. 104305.

[84] Danoun, A., E. Prulière, and Y. Chemisky, *Thermodynamically consistent Recurrent Neural Networks to predict non linear behaviors of dissipative materials subjected to non-proportional loading paths.* Mechanics of Materials, 2022. **173**: p. 104436.

[85] Haghighat, E., et al., *A physics-informed deep learning framework for inversion and surrogate modeling in solid mechanics.* Computer Methods in Applied Mechanics and Engineering, 2021. **379**: p. 113741.

[86] Abueidda, D.W., et al., *Deep learning for plasticity and thermo-viscoplasticity.* International Journal of Plasticity, 2021. **136**: p. 102852.

[87] Yang, Y.-L., *A study of inelastic/anelastic behaviour and springback of AA7050 alloy in creep age forming*, in *Mechanical Engineering*. 2017, Imperial College London: London.

[88] Dugas, C., et al., *Incorporating Functional Knowledge in Neural Networks.* J. Mach. Learn. Res., 2009. **10**: p. 1239–1262.

[89] Abbo, A.J. and S.W. Sloan, *A smooth hyperbolic approximation to the Mohr-Coulomb yield criterion.* Computers & Structures, 1995. **54**(3): p. 427–441.